Mechanism and Machine Theory 181 (2023) 105216

Contents lists available at ScienceDirect

Mechanism and Machine Theory

journal homepage: www.elsevier.com/locate/mechmt

Research paper

# Use of sun gear orbits to obtain the load sharing in planetary transmissions and its impact in the tooth load

J. Sanchez-Espiga, A. Fernandez-del-Rincon, M. Iglesias, F. Viadero *

*Departamento de Ingeniería Estructural y Mecánica, ETSIIT Universidad de Cantabria, Avda. de los Castros s/n 39005 Santander, España*

ARTICLE INFO

*Keywords:*
Esh phasing
Sun gear orbits
Load sharing
Contact forces per tooth
Planetary transmissions

ABSTRACT

The present work assesses the possibility of using the orbits described by the sun gear in order to analyse the load sharing ratio in planetary gear transmissions. Furthermore, the current work is extended to observe the impact of the floatability and different tangential pinhole position errors in the load borne in a single contact between a pair of teeth in comparison to the load per planet. Therefore, it highlights the inaccuracy of the load sharing ratio (LSR) as an indicator of the overload in one tooth of the planet. Moreover, the use of the orbits represented with respect to a rotating reference provides helpful information to determine the overloads and underloads in the planets due to the existence of a tangential error in sequentially phased transmissions. Therefore, this proposal provides a simpler solution to the measurement of the LSR in planetary transmissions with different numbers of planets than the use of strain gauges.

## 1. Introduction

Power transmissions play a crucial role in the industry. Among the possible transmissions, gear transmissions are one of the most common solutions. Within the scope of possible gear transmissions, planetary transmissions present a number of advantages compared to others. These are more robust, compact and have a higher power density than analogous conventional transmissions. Furthermore, the coaxiality between input and output together with the previous advantages makes them more suitable for applications in wind generators [1,2], electric vehicles [3], and helicopters [4,5] among others.

Given the several applications for planetary gearboxes, in the recent decades there has been a sky-rocketing increment in the number of publications [6] and in the development of new models. Modelling in gear transmissions and, more precisely in planetary transmissions, can be classified based on the approach taken in each model. This all started by analytical approaches [7] and lumped-parameter models, which are still a considerably accurate tool [8–13]. Nonetheless, this is not the only valid approach, other authors opted for finite-element (FE) models [14–16] or hybrid approaches combining proposals [17–21].

Thus, derived from the development of these models several research works have been presented regarding the load sharing, the meshing stiffness [10,18,22–24] and contact forces [25–27] in planetary gear transmissions. These works focus on the impact that various effects have in the performance of such a transmission, errors [28,29], misalignments [12,30,31], gravity [32–34], eccentricities [28,35], to name a few.

Regarding the study of the orbits described by the different gears or even the planet carrier, several approaches have been presented. On the one hand, a number of models provide the possibility of including floatability in different elements as in [32,36–39] among others. On the other hand, some other authors developed different procedures to perform an experimental validation of the

* Corresponding author.

https://doi.org/10.1016/j.mechmachtheory.2022.105216
Received 7 October 2022; Received in revised form 9 December 2022; Accepted 21 December 2022
Available online 28 December 2022

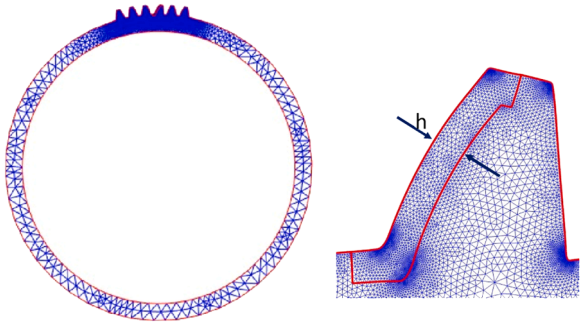


**Fig. 1.** Global and local FE models of the sun gear with deflections due the load applied.

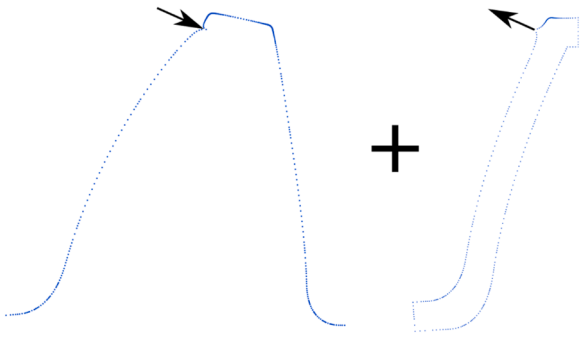

**Fig. 2.** Application of the superposition principle in the global and local FE models, the deflected profile of the models is presented with the applied load.

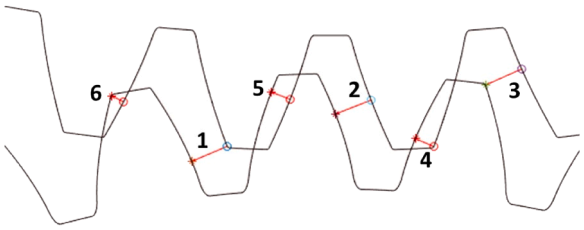


**Fig. 3.** Detail of possible contacts considered by the model with the actual overlaps in a red solid line.

orbits [36,40–42]. These works focus on the impact of the stiffness in the supports and rotating components and mainly its dynamical response to different working situations.

The current work presents a previously validated 2-D model for planetary spur gears [19] developed to simulate a series of experiments allowing the definition of simplified simulation environments. The choice of a 2-D model is supported by the fact that they have been proved to be a suitable and powerful tool for previous studies in the recent years such as [9,13,23,43]. These 2-D formulations allow to exclude some three-dimensional effects that are less relevant in approaches as the one presented in this work, enabling to reduce the computational cost of the simulations without reducing the accuracy. Furthermore, these more computationally-efficient approaches allow the statistical analysis of results by the definition of a significant number of simulation scenarios changing different working parameters such as the number of planets, the mesh phasing, and the planet spacing among others. A considerable number of simulations generates the definition of trends in the results.

This work proposes the analysis of the contact forces per tooth in comparison with the amount of load borne by each planet. Despite the fact that the contact forces do not count with a standardized procedure to be validated, the amount of load in each gear can be extrapolated from the deflection in some strain gauges, as seen in [41,42,44–46]. Regarding this point, this model has been employed previously in the analysis of the trends followed by the deformations suffered by strain gauges placed on the tooth root [47,48] to analyse the discrepancies between the experimental and modelling results shown in [44]. However, there is not a consensus on the most suitable approach for the use of strain gauges to obtain the load sharing in a planetary transmission, they can be placed in the sun gear [44,45], planet pins [41,42] or ring gear [45,46]. Therefore, in this work, the previously mentioned model is extended aiming to use the orbit described by the sun gear centre in order to assess the load sharing in a planetary transmission.

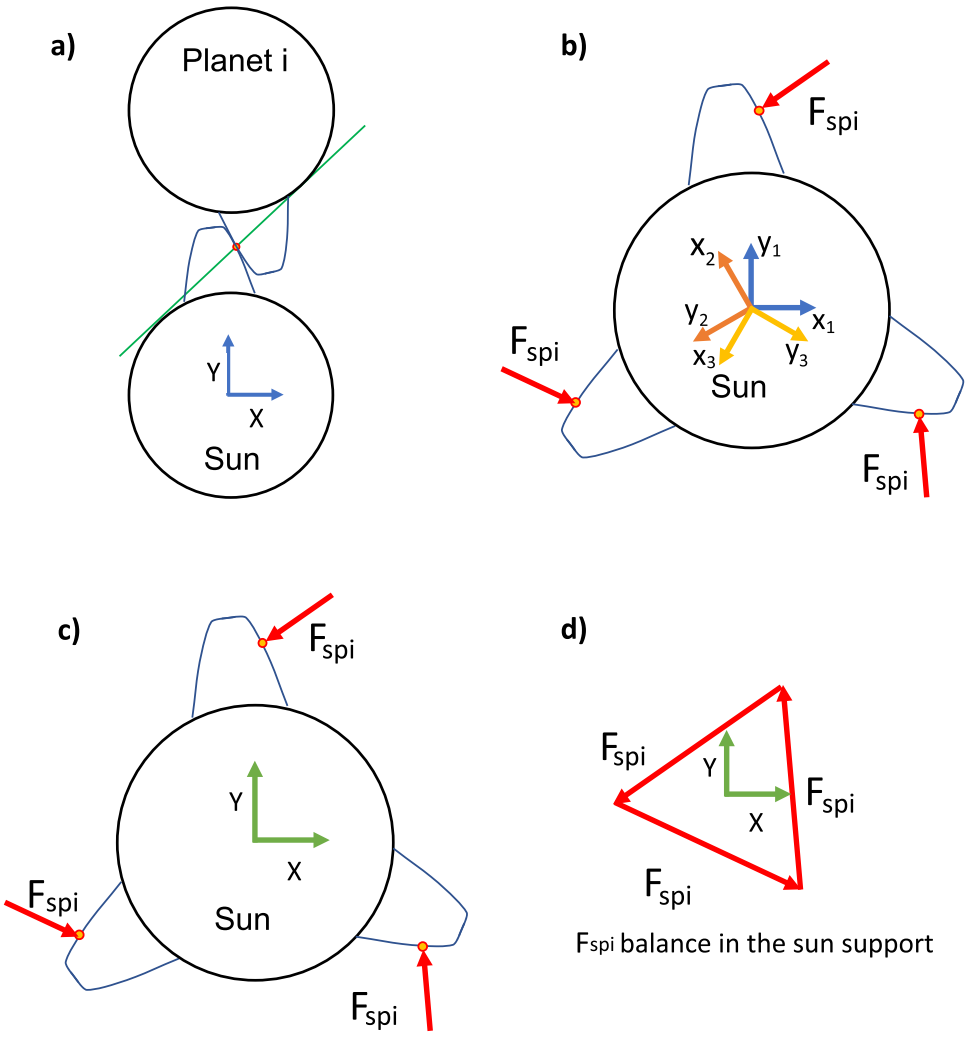


**Fig. 4.** Coordinate systems in the model: a) local frame, b) local frames in the transmission, c) fixed general coordinate frame and d) balance in the sun support for the general coordinate frame.

The interest of this study comes from the visible difference between the load supported by one tooth alone and the amount of load supported by the gear, thus, the load sharing is not an accurate parameter to observe the load supported by each tooth and, consequently, its durability. Furthermore, the new proposal to the measurement of the orbits aims to assess the possibility that this may be a simpler viable option to induce the load sharing in a planetary transmission apart from the normal use of strain gauges to perform experimental measurements and calculate the load sharing in a planetary transmission.

Therefore, this manuscript is structured in a number of sections, where Section 2 gathers all the description regarding the model employed for this work. Afterwards, Section 3 compiles the configurations that are considered interesting to this aim. Then, in Section 4 the results both for the orbits described by the sun gear (Section 4.1) and the contact forces (Section 4.2).

Finally, Section 5 presents the conclusions fruit of the analysis of the results.

## 2. Model

In the current section the different details of the model that are relevant for this manuscript are explained. The focus, given the topic of the present work, is on the contact problem, the impact of the tangential errors and the stiffness included in the sun support.

### *2.1. Contact location and calculation*

Firstly, the contact solution implemented in the model used for this work [19] combines a couple of finite element models derived from [15] with an analytical approach [49] in order to solve the non-linear local contact.

The algorithm employed to solve the contact between active flanks consists of two different formulations that work in parallel,

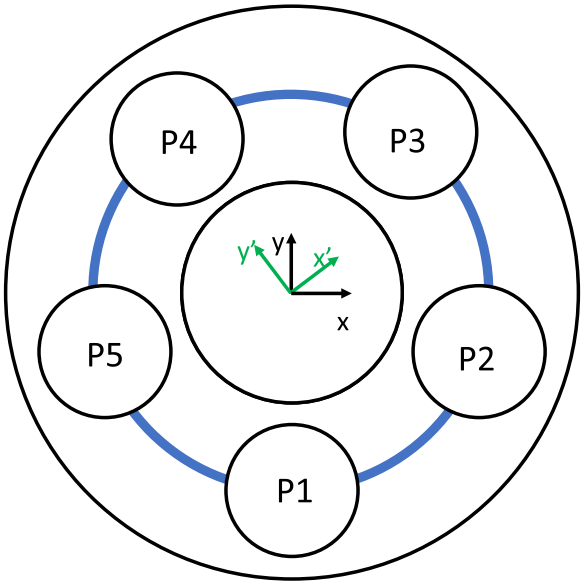


**Fig. 5.** Diagram of a 5-planet transmission with the numbering of the planets (P1-P5) and fixed and rotating coordinates systems used for the orbits.

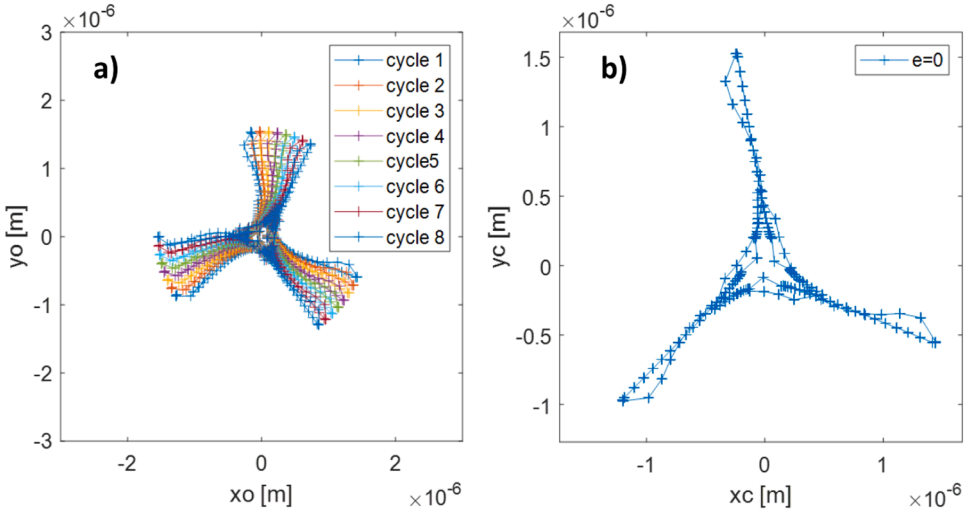


**Fig. 6.** 3-planet ESSP sun orbits: a) fixed reference b) rotating reference.

there is a linear algorithm that solves the linear part of the contact, and a non-linear formulation for the local contact in the area next to the contact point. On the former, a FE model (Fig. 1) is used to represent the body of the gear and a number of teeth, as seen in [47,50,51]. This model will be known from this point on as the global model. Thus, the global model is a planar FE model meshed using triangular elements with nodes in each vertex, using the Partial Differential Equations Toolbox in MATLAB. Regarding the boundary conditions, all the geometry related to the shaft mounting is considered embedded. Then, there is another FE model (Fig. 1) that represents only the geometry of the active flank to a depth of h, this will be referred as local model onwards. This model is meshed analogously to the global one. In terms of boundary conditions, the embedment spreads along the line that represents the interface between this model and the rest of the tooth. Therefore, by applying in this models the same load in the same point of the tooth profile, however, in opposite directions, it is possible to obtain the deformations in the teeth and body of the gear. This is based on using the superposition principle, as shown in Fig. 2. As a result, the model provides the deformations on the body of the gear and the represented teeth due to the action of a unitary force in a specific point along the profile. This approach allows to eliminate the distortion in the deformations due to the use of a point force [18,19].

Regarding the local contact, Weber-Banaschek's approach, proposed in [49], is taken for external gears contact and modified by Iglesias et al. in [19] for the internal gears. This Hertzian approach provides the deformations suffered by a point inside the tooth due to the contact in the active flanks. Thus, by combining the previous FE models and this analytical approach it is possible to know the

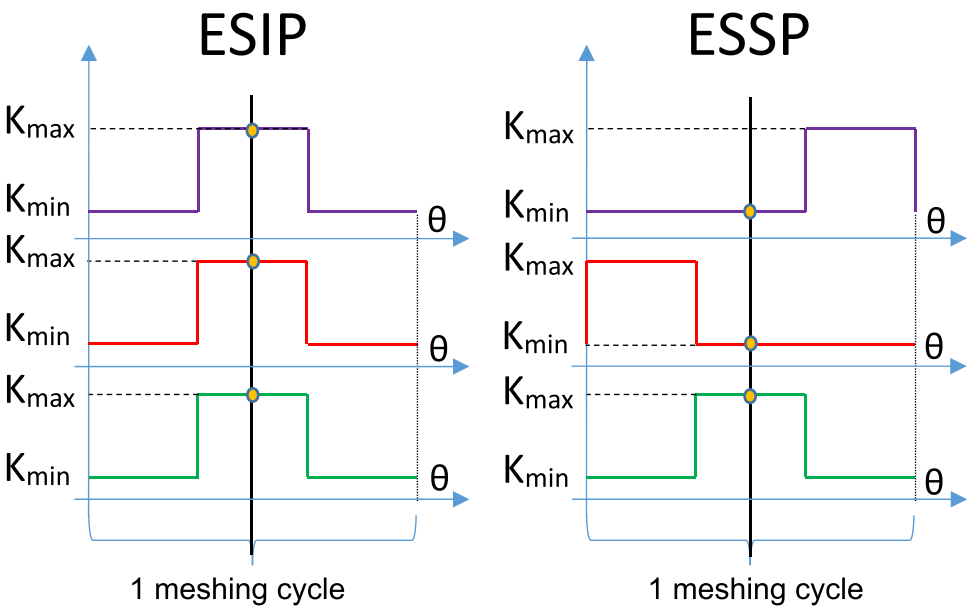


**Fig. 7.** Diagram of the meshing stiffness for ESIP and ESSP transmissions.

**Table 1**
Geometrical specifications of the teeth profiles.

| Parameter | Value |
|---|---|
| Module (mm) | 4.5 |
| Pressure angle (°) | 20 |
| Addendum (mm) | 4.5 |
| Dedendum (mm) | 5.625 |
| Tip rounding arc radius (mm) | 0.225 |

**Table 2**
Number of teeth for each gear in the considered transmissions, the values are included following the standard set by the ISO-21771.

| *N* | Configuration | $Z_r$ | $Z_p$ | $Z_s$ |
|---|---|---|---|---|
| 3 & 5 | ESIP | −165 | 44 | 75 |
| | ESSP | −166 | 45 | 74 |
| 4 | ESIP | −164 | 43 | 76 |
| | ESSP | −166 | 45 | 74 |

**Table 3**
Input torque in the sun gear with the number of planets and reference force.

| | | Reference force (N) | |
|---|---|---|---|
| *N* | Torque (Nm) | ESIP | ESSP |
| 3 | 1200 | 2522.5 | 2556.6 |
| 4 | 1600 | 2489.3 | 2522.6 |
| 5 | 2000 | 2522.5 | 2556.6 |

**Table 4**
Tangential pinhole position error in one of the planets.

| Transmission configuration | Tangential error ($\mu m$) | | | | |
|---|---|---|---|---|---|
| ESIP | 0 | 1.25 | 2.5 | 3.75 | 5 |
| ESSP | 0 | 1.25 | 2.5 | 3.75 | 5 |

**Table 5**
Sun support stiffnesses in the studied configurations.

| Transmission configuration | Sun support stiffnesses (N/m) | |
|---|---|---|
| ESIP | 1e8 | 1e6 |
| ESSP | 1e8 | 1e6 |

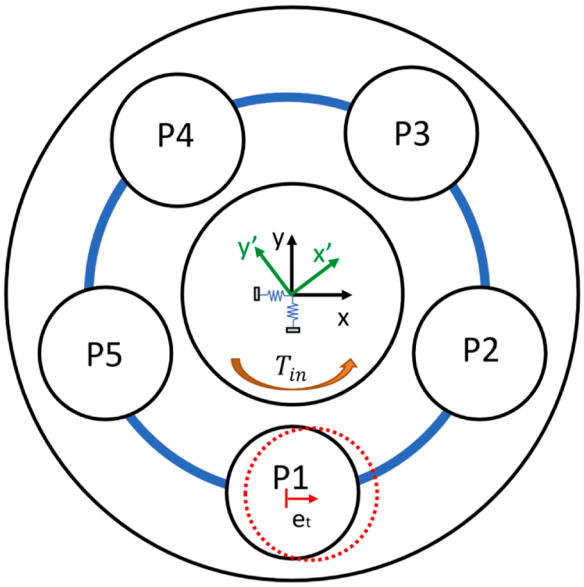


**Fig. 8.** Fixed (in black) and rotating (in green) coordinates systems.

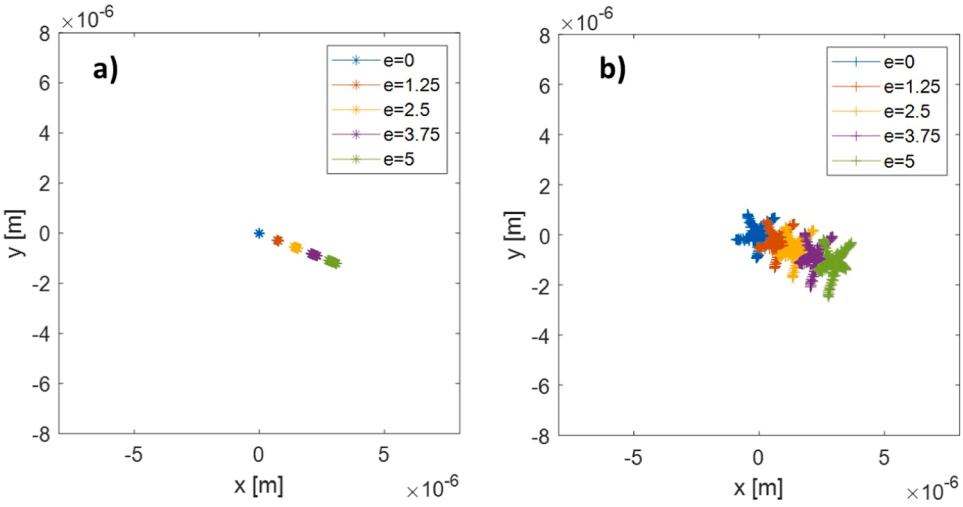


**Fig. 9.** 3-planet transmissions comparison of the orbits for every tangential error (0, 1.25, 2.5, 3.75, 5 $\mu m$): a) ESIP, b) ESSP.

stiffness of the teeth and the body of the gears.

On the other hand, this model supposes that the gears can overlap, in fact, at the beginning of the calculation the wheels are forced to overlap, as shown in Fig. 3. Thus, by calculating the geometrical overlap between pairs of teeth it is possible to locate the active contacts. The number of possible contacts that are considered depend on the contact ratio ($\varepsilon$), and is calculated by using Eq. (1).

$$N_c = 2 \cdot ceil\,(\varepsilon + 1) \tag{1}$$

Thus, for a contact ratio between 1 and 2, the most common situation in spur gears, the number of possible contacts is 6. This is shown

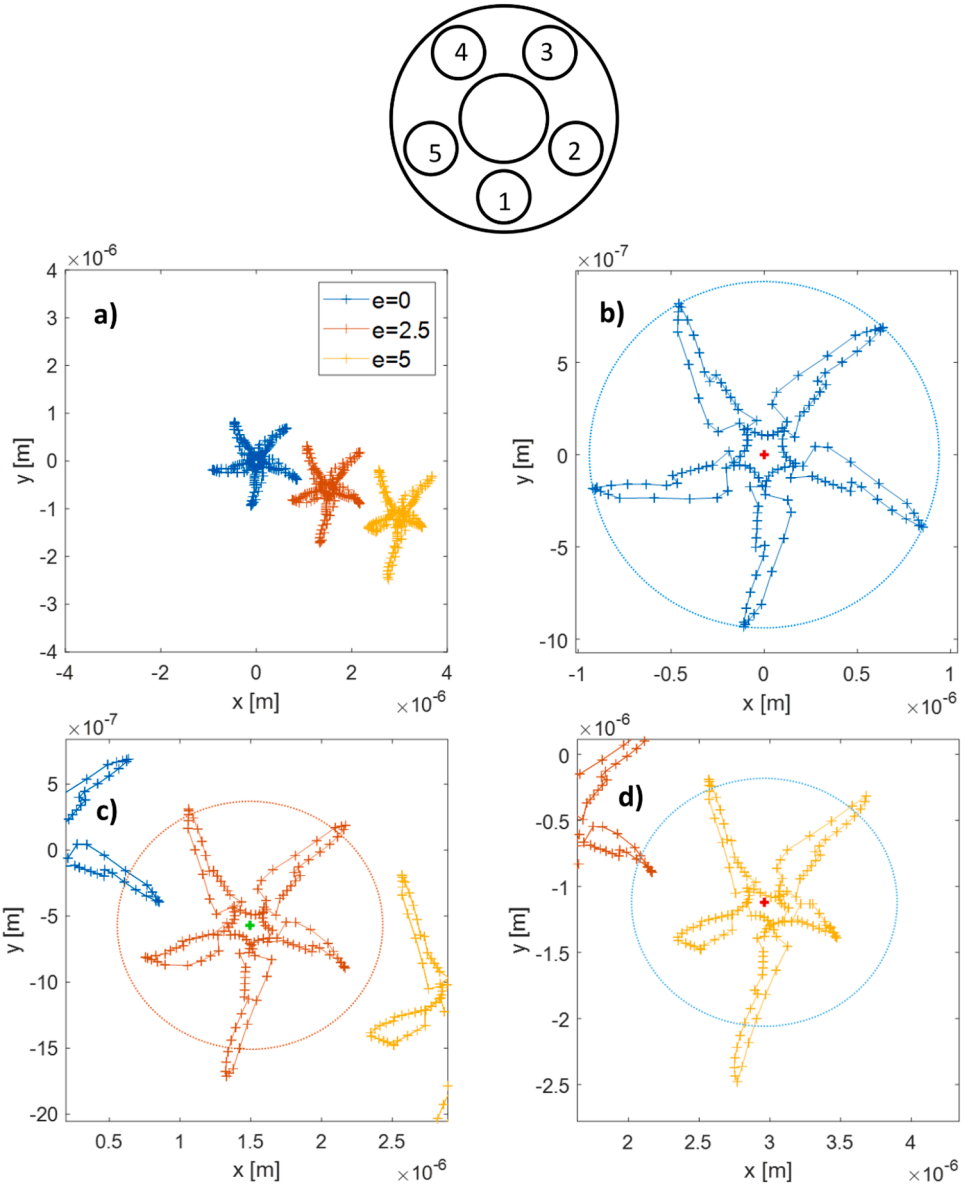


**Fig. 10.** Sun orbits of 5-planet ESSP transmission with 1e8 N/m stiffness: a) 0, 2.5 & 5 $\mu m$ b) 0 $\mu m$ c) 2.5 $\mu m$ d) 5 μm.

**Table 6**
Results of maximum in the load sharing for ESSP 5-planet transmission for 1e8 N/m stiffness.

| | Planet 1 | Planet 2 | Planet 3 | Planet 4 | Planet 5 |
|---|---|---|---|---|---|
| max.$LSR@e_t[0]$ | 0.2181 | 0.2181 | 0.2181 | 0.2181 | 0.2181 |
| max.$LSR@e_t[2.5]$ | 0.1771 | 0.2444 | 0.2128 | 0.2115 | 0.2478 |
| max.$LSR@e_t[5]$ | 0.1382 | 0.2704 | 0.2075 | 0.2068 | 0.2763 |

in Fig. 3.

The calculation of the overlaps, which are shown exaggeratedly in Fig. 3 by a solid red line between o and * icons, will make difference between different sections along the profile of the gear teeth. Thus, the contact algorithm considers the possibility of involute-involute contact or involute-tip-rounding-arc or tip-rounding-arc-involute contact. The criteria used to differentiate each contact is the pressure angle ($\varphi$). The expressions used for the calculation of the overlap can be found in [19] & [51].

Finally, by combining the overlaps and the stiffnesses of the gears, it is possible to obtain the contact forces and solve the balance in the transmission, as shown in [51].

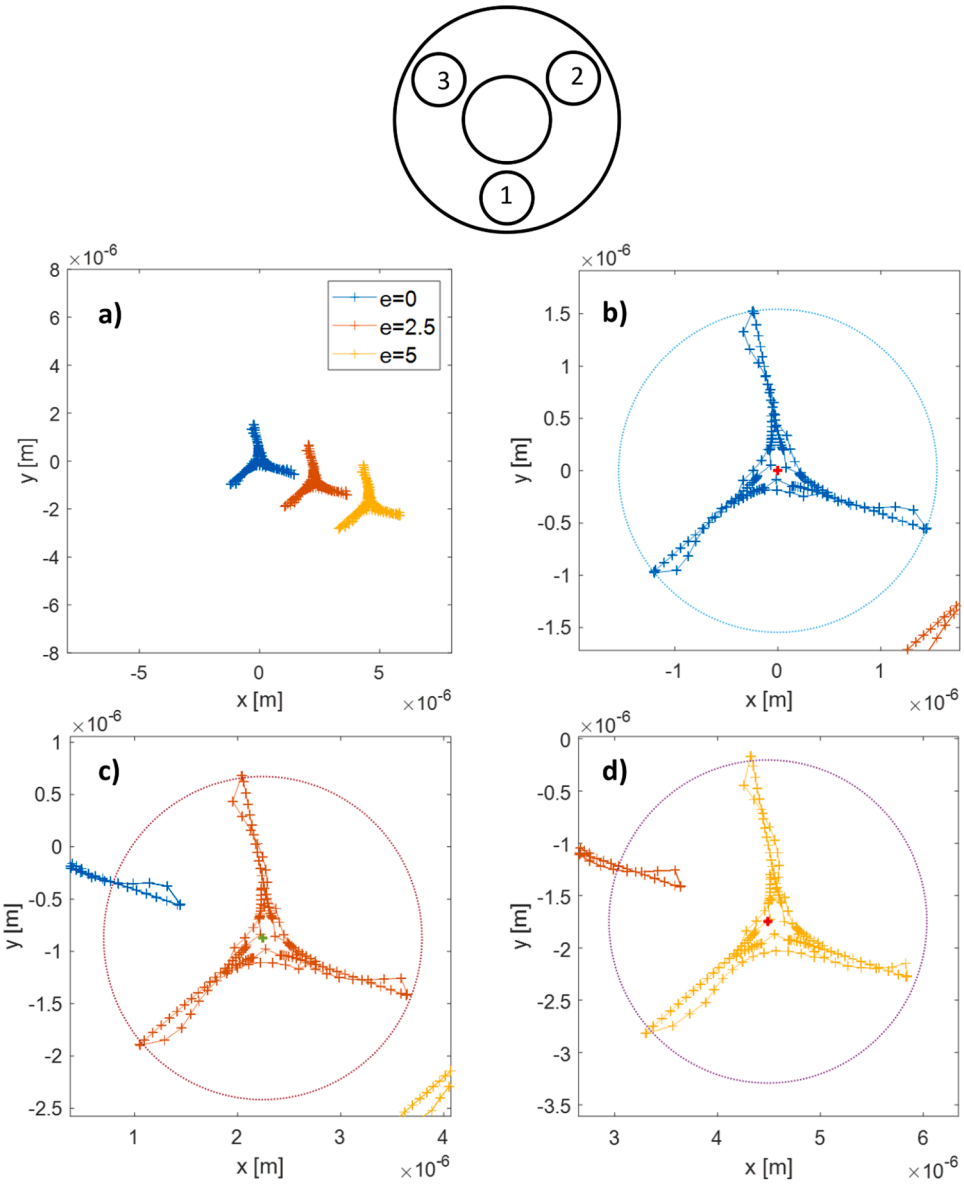


**Fig. 11.** Sun orbits of 3-planet ESSP transmission with 1e8 N/m stiffness: a) 0, 2.5 & 5 $\mu m$ b) 0 $\mu m$ c) 2.5 $\mu m$ d) 5 µm.

### 2.2. *Rotating reference for the sun gear orbit*

In the current work, the 2D-model by Iglesias et al. [19] is reformulated looking for obtaining a new approach to the measurement of the sun gear orbit. Firstly, it is relevant to comment this model solves the contact problem per pair of wheels. Thus, every sun-planet and planet-ring contacts are solved independently and then balance in the system is searched. Therefore, focusing on every sun-planet contact, the coordinate frame shown in Fig. 4a) shows the local coordinate system employed to any of these contacts. This local coordinate frame is defined always with the y axis in the direction of the centre distance between sun and planet. Then, the x axis is transversal to the previous one. Therefore, Fig. 4b) presents the local coordinate systems for each sun-planet contact in a 3-planet transmission from the general configuration of the transmission. In this coordinate frames every contact force, presented as $F_{spi}$ is exactly the same in an ideal in-phase planetary transmission without error. However, in order to obtain the balance in the transmission these contact forces are referred to a fixed general coordinate frame, presented in Fig. 4c). Thus, the results are not identical, but provide a balance in the sun gear support, as shown in Fig. 4d).

Regarding the balance in the sun support, the contact forces are rotated from the local frame, in which they are calculated, to the general fixed frame, used for the balance problem in the transmission. Thus, this provides a vector system that allows to observe any imbalance, and for configurations with stiffness in the support the wheel modifies its position in order to erase or diminish the

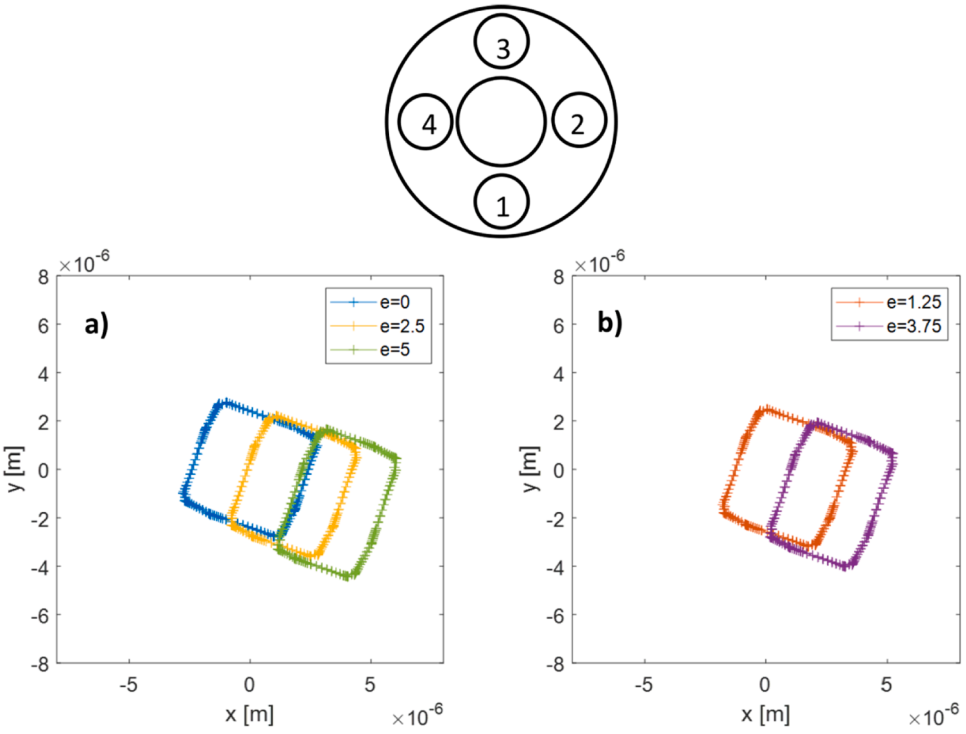


**Fig. 12.** 4-planet ESSP transmission 1e8 N/m stiffness, sun orbits for every considered error: 0, 2.5 & 5 $\mu m$ (left) 1.25 & 3.75 $\mu m$ (right).

**Table 7**
Results of maximum in the load sharing for ESSP 3-planet transmission for 1e8 N/m stiffness.

| | Planet 1 | Planet 2 | Planet 3 |
|---|---|---|---|
| max.$LSR@e_t[0]$ | 0.3402 | 0.3402 | 0.3402 |
| max.$LSR@e_t[2.5]$ | 0.319 | 0.351 | 0.3509 |
| max.$LSR@e_t[5]$ | 0.2978 | 0.3619 | 0.3618 |

**Table 8**
Results of maximum in the load sharing for ESSP 4-planet transmission for 1e8 N/m stiffness.

| | Planet 1 | Planet 2 | Planet 3 | Planet 4 |
|---|---|---|---|---|
| max.$LSR@e_t[0]$ | 0.2824 | 0.2823 | 0.2824 | 0.2823 |
| max.$LSR@e_t[1.25]$ | 0.2636 | 0.2960 | 0.2743 | 0.2955 |
| max.$LSR@e_t[2.5]$ | 0.2450 | 0.3095 | 0.2663 | 0.3088 |
| max.$LSR@e_t[3.75]$ | 0.2262 | 0.3230 | 0.2583 | 0.3221 |
| max.$LSR@e_t[5]$ | 0.2076 | 0.3368 | 0.2503 | 0.3354 |

imbalance in the contact forces, and consequently, in the load sharing of the transmission. The movement of the centre of the wheel to absorb the imbalance also leads it to describe an orbit around its initial mounting position. Normally, the sun gear orbits are measured from a fixed reference, as seen in [32,36–39]. However, in this proposal the formulation of the balance problem, shown in [38], has been modified in order to obtain the orbit from a rotating reference, shown in Fig. 5 in green together with the numbering assigned to the planets (P1-P5) that is used also for the results presented in Section 4. The mentioned green reference rotates along with the planet carrier.

The approach proposed consists in recreating the measurement of a probe embarked in the planet carrier of a planetary transmission to be able to measure the changes in the position of the sun gear centre from a rotating reference. To this aim, firstly, two effects are visible in the orbit described by the sun. First of all, there is a variation of the orbit due to the change in each sun-planet contact, this generates a loop around an equilibrium position. Secondly, there is also a rotation around the initial mounting position due to the rotation of the planet carrier. By embarking the probe on the carrier, the effect will be that the relative movement of the planets around the sun will not be visible for an observer situated on the planet carrier, therefore, the effect of the planet carrier rotation will disappear in the measurement of the sun orbit. In order to develop this proposal and erase the effect of the planet carrier

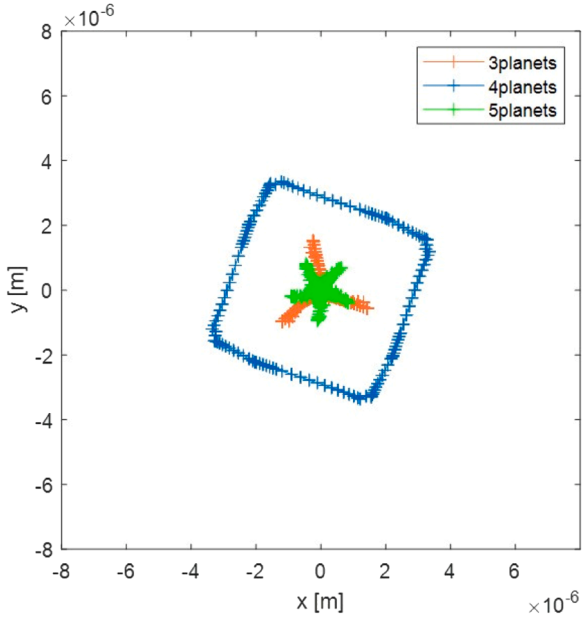


**Fig. 13.** Comparison of ESSP transmissions orbits with the number of planets, for configurations without tangential error.

rotation in the measured sun gear orbit, the rotation matrix to convert the local coordinate frames to the general coordinate frames is Eq. (2), where only the planet spacing ($\psi_i$) is considered. Then, following Eqs. (3) & (4) the vector system in the sun gear support is obtained, eliminating the effect of the planet carrier rotation.

$$\mathbf{R} = \begin{bmatrix} \cos(\psi_i) & \sin(\psi_i) \\ -\sin(\psi_i) & \cos(\psi_i) \end{bmatrix} \tag{2}$$

$$\overrightarrow{F}_{spigen} = \overrightarrow{F}_{spiloc} \wedge R \tag{3}$$

$$\overrightarrow{F}_{s} = \sum_{i=1}^{N} \overrightarrow{F}_{spigen} \tag{4}$$

In the equations above $\overrightarrow{F}_{spigen}$ & $\overrightarrow{F}_{spiloc}$ refer to the contact force between sun and planets in the general and local coordinate frames respectively. Then, the $\overrightarrow{F}_{s}$ refers to the force in the support of the gear due to the balance among the contact forces. In Fig. 6 the sun gear orbit in a 3-planet Equally Spaced Sequentially Phased (ESSP) planetary transmission are compared with a measurement from a fixed reference and a rotating reference. In both of them 8 meshing cycles completed by the sun have been represented.

Observing Fig. 6, some advantages can be highlighted of this new method:

- The orbit is a closed loop for each meshing cycle, in case there is not a time varying effect. Any of these loops represents the change in the position of the sun gear centre only due to the evolution of its contacts with the planets.
- If every contact is equal, every single loop overlaps with the previous and all of them are identical. Thus, it is possible to observe any irregularity in any of the meshing cycles, given the fact that, the overlap between loops would not be perfect in such case.
- It allows to infer the load sharing in the ESSP transmissions by studying the change in the shape of the loops described by the sun gear in a meshing cycle.
- These advantages will be highlighted and described in more detail in Section 4.1 by comparing the results with the previous approach and this new proposal and extending the analysis to all the scenarios presented in 3.

## 3. Considered configurations

In this section the working parameters included in the simulations are established. Firstly, the characteristics of the profiles of every teeth and the number of teeth in each configuration for Equally Spaced In-Phase (ESIP) and ESSP transmissions. In order to illustrate the impact that the mesh phasing has in the performance of the transmission and the scope covered by choosing these configurations, in Fig. 7 the variability of the meshing stiffness in any meshing cycle for both kinds of transmissions is shown in a pair of diagrams. Therefore, the meshing stiffness in each case varies within a minimum ($K_{min}$) and a maximum ($K_{max}$) value, which are equal for every planet. However, in this case, they have been separated to avoid overlapping and ease the understanding of the figure. Besides, these

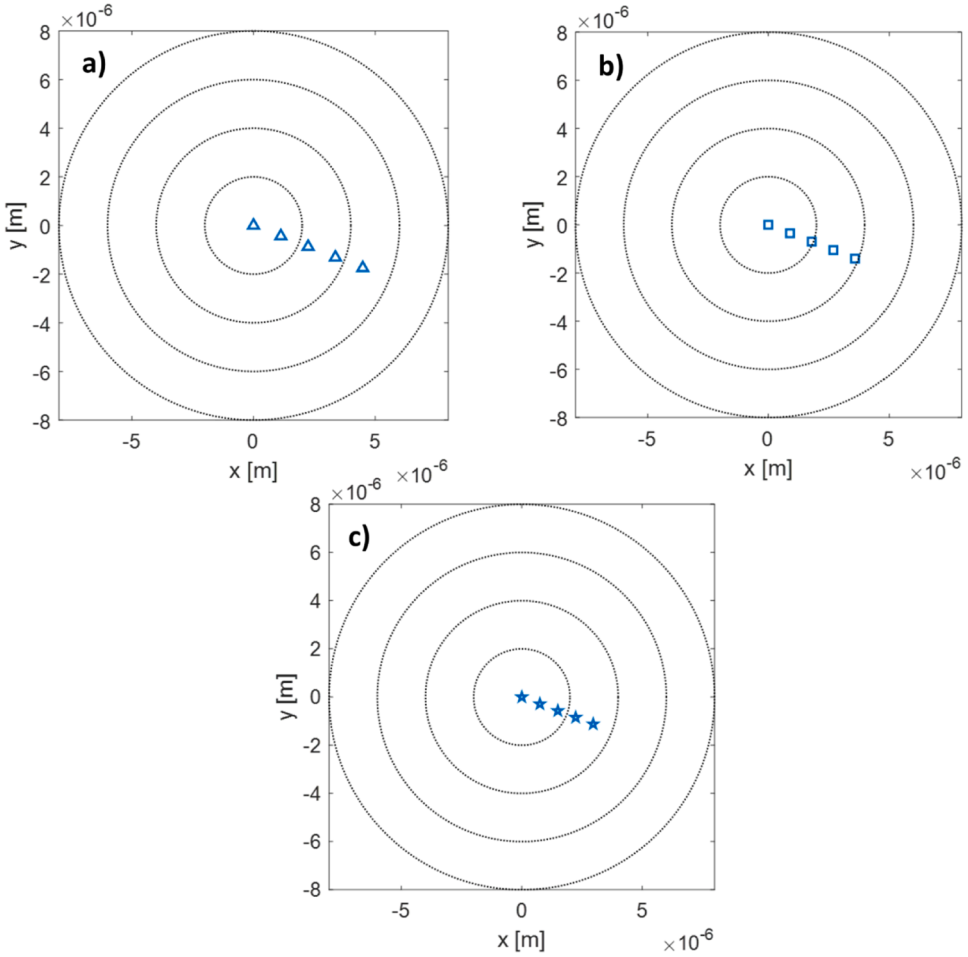


**Fig. 14.** Comparison of the change in the position of the orbit centroid for all the cases considered in each transmission ($e_t$: 0, 1.25, 2.5, 3.75, 5 μm): a) 3 planets, b) 4 planets, c) 5 planets.

diagrams show how for a ESIP transmission the meshing stiffness is exactly the same for each planet, at any given moment, one of which is selected with an orange dot. On the other hand, the meshing stiffness in a ESSP transmission varies with a delay between planets and therefore the meshing stiffness in each planet will not be identical to the rest. For these diagrams the reader should take into account that no effects of any error were considered and the shape of the meshing stiffness has been simplified.

The number of planets ($N$) that are considered are 3, 4 & 5. Thus, Tables 1 and 2 gather all the information regarding these points.

Regarding the input torque applied in the sun gear, this has to be adapted to the number of planets looking for similar contact forces in every scenario, and therefore, similar deflections and orbits independently to the number of planets. The input torque values used are gathered in Table 3.

The reference force refers to the contact force in a planet due to an even distribution of the input torque among all the branches present in a planetary transmission. This stands for the transmissions in ideal conditions, which means that the transmission is perfectly balanced and no manufacturing error is considered. Thus, this is calculated by using Eq. (5) and as the number of teeth ($Z_s$) in each sun varies, so does the base radius ($r_{si}$) and the reference force ($F_{ref}$). However, these variations are slight and unavoidable due to the necessary change on the number of teeth in order to study the different configurations and both mesh phasing options.

$$F_{ref} = \frac{T_{in}}{N \cdot r_{si}} \tag{5}$$

Finally, tangential pinhole position errors are included in one of the planets mounting for each transmission. The error is modelled by modifying the mounting position of the planet. In this case, a tangential error will be applied in the horizontal direction, tangential to the planet carrier. It is necessary to consider this modification when setting the rotations of the gears for the previously mentioned initial overlap. This error will modify those overlaps. More details regarding this point are shown in [51]. This error has been chosen given their significant influence, as shown in previous works [51]. Thus, Table 4 gathers every error considered. The size of the errors are the same for every transmission looking for comparable effects in each. Furthermore, the size of the errors is not significantly big looking for avoiding the loss of contact, but having enough scenarios to observe the trends followed by the results with the size of the

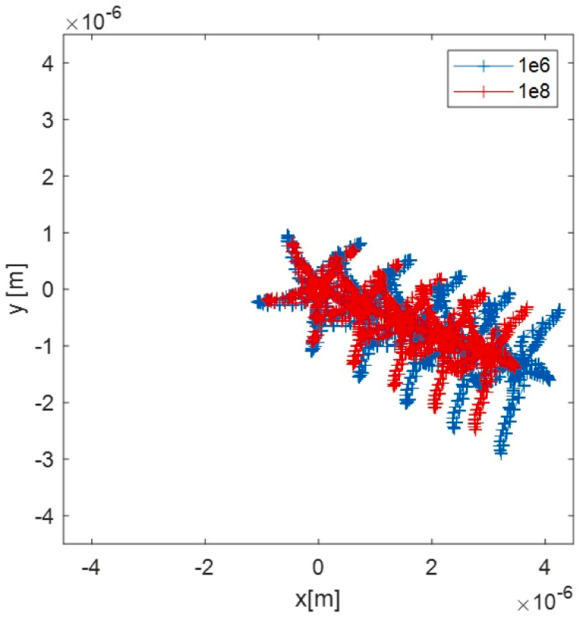


**Fig. 15.** 5-planet ESSP transmission sun orbits with 1e8 and 1e6 N/m sun support stiffness.

error.

Besides, another effect that is considered is the stiffness in the sun support. Thus, in Table 5 two different levels of stiffness are considered. The first stiffness (1e8 N/m) is chosen by following previous works [20,26,32] and looking for a simplified approach that allows including this effect and does not increase significantly the computational cost. Therefore, it is modelled following a lumped-parameter formulation and establishing the same stiffness in the x and y directions, following the fixed reference presented in Fig. 8. The second level of stiffness (1e6 N/m) is chosen following [52], more precisely, it refers to a reduction of two orders of magnitude from the initial support stiffness in order to approximate the floating sun gear configuration. However, for the 3 planet configuration the 1e6 N/m stiffness is not considered due to the inherent self-balancing effect present in the 3-planet transmissions with a floating sun.

In Fig. 8 a diagram of a 5-planet transmission is presented to show all the effects considered in the simulations and provide the reference taken for the numbering of the planets P1-P5. This pattern is followed also for 3 and 4-planet transmissions reaching up to P3 or P4 respectively. Besides, in a dotted red line the position of the planet with the tangential error is shown. This planet will be the one including the tangential error in all the studied scenarios.

All in all, this work presents 3 different number of planets ($N$), 2 mesh phasing options for each, 5 sizes for the tangential pinhole position errors ($e_t$), and 2 stiffness levels for the sun support. Thus, the results of a total of 55 simulations, excluding the ones for 3-planet transmission with 1e6 stiffness, are presented in this work.

## 4. Results

This section gathers all the results to the simulations mentioned before in Section 3. However, this section has been divided in two subsections in order to study separately the orbits described by the sun in every scenario, and the contact forces in each tooth and planet.

### 4.1. Sun orbits

In this subsection the results to the new representation of the orbits are compared with the classical approach to this problem. Besides, the growth and variation of the orbits with the tangential error is presented.

First of all, the difference between the conventional orbit and the new representation system are presented in Fig. 6 in Section 2.2. To this aim, the scenario chosen is the 3-planet transmission ESSP without tangential error. Thus, the orbit is uniform, presents a perfect repeatability, and describes a number of loops equal to the number of planets due to the sequential contact with each planet. The simulations are performed for 8 meshing cycles in the sun, thus, the carrier does not complete a whole rotation, but it is possible to establish the differences between methods.

Once these differences are established, the following study is focused on the analysis of the orbits by using the new representation system. To this aim, Fig. 9a) presents the orbits described by the sun in the ESIP transmission considering all the cases of tangential error in the planet 1, which were specified previously in Table 4. Likewise, Fig. 9b) present the same results for the ESSP transmission.

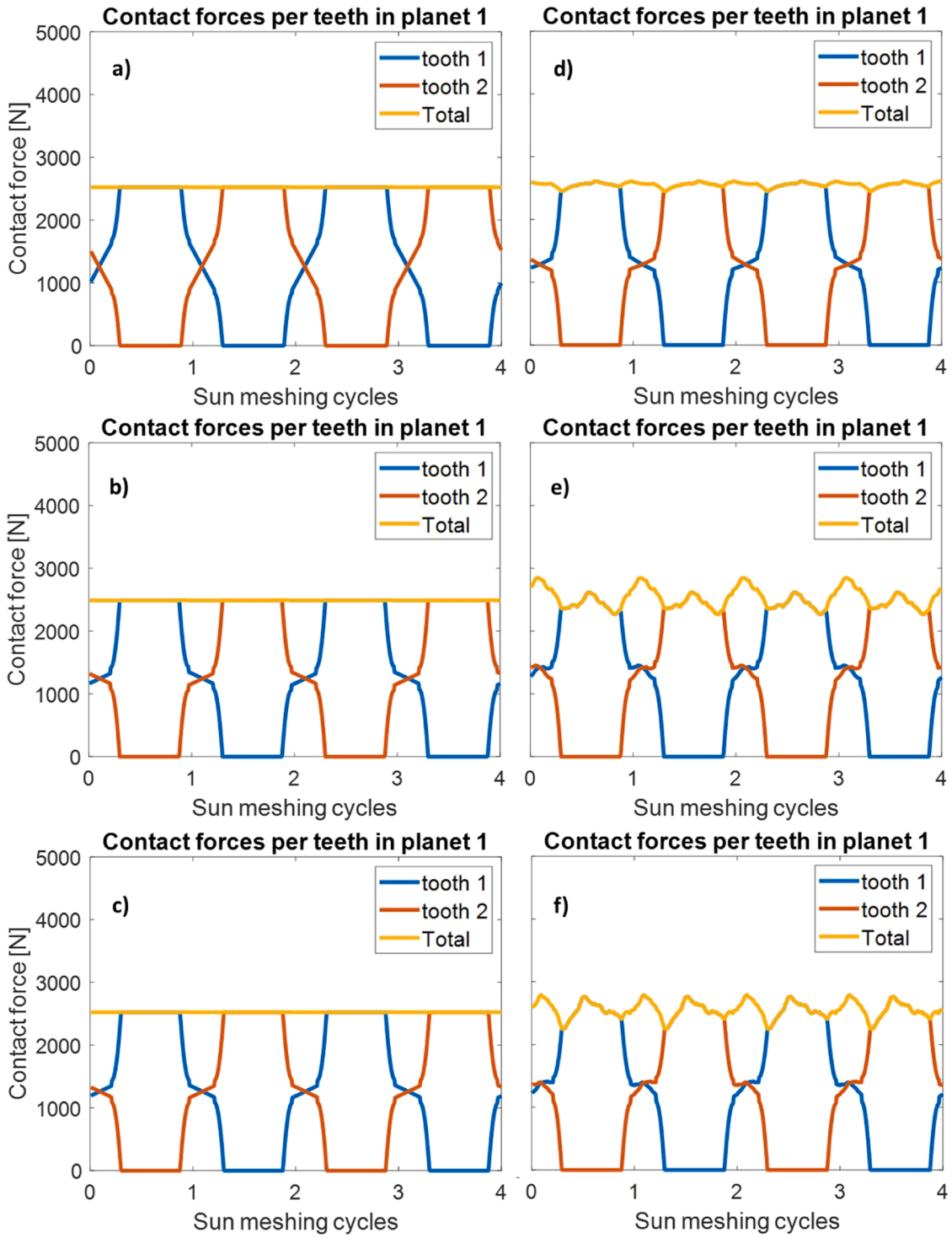


**Fig. 16.** ESIP (left) & ESSP (right) transmissions 1e8 N/m: a & d) 3-planet b & e) 4-planet c & f) 5-planet.

In both kinds of transmissions the errors included are the same and they are included in the same planet pin.

Therefore, a growth in the translation of the sun centre is visible for ESIP and ESSP transmissions with the growth of the tangential error. Then, the size of the orbit described by the sun around this translation position for the ESIP transmission also grows with the error, however, it is insignificant compared to the size of the orbit for the ESSP transmission.

On the other hand, regarding one of the advantages of this new representation that were highlighted in Section 2.2 the best example

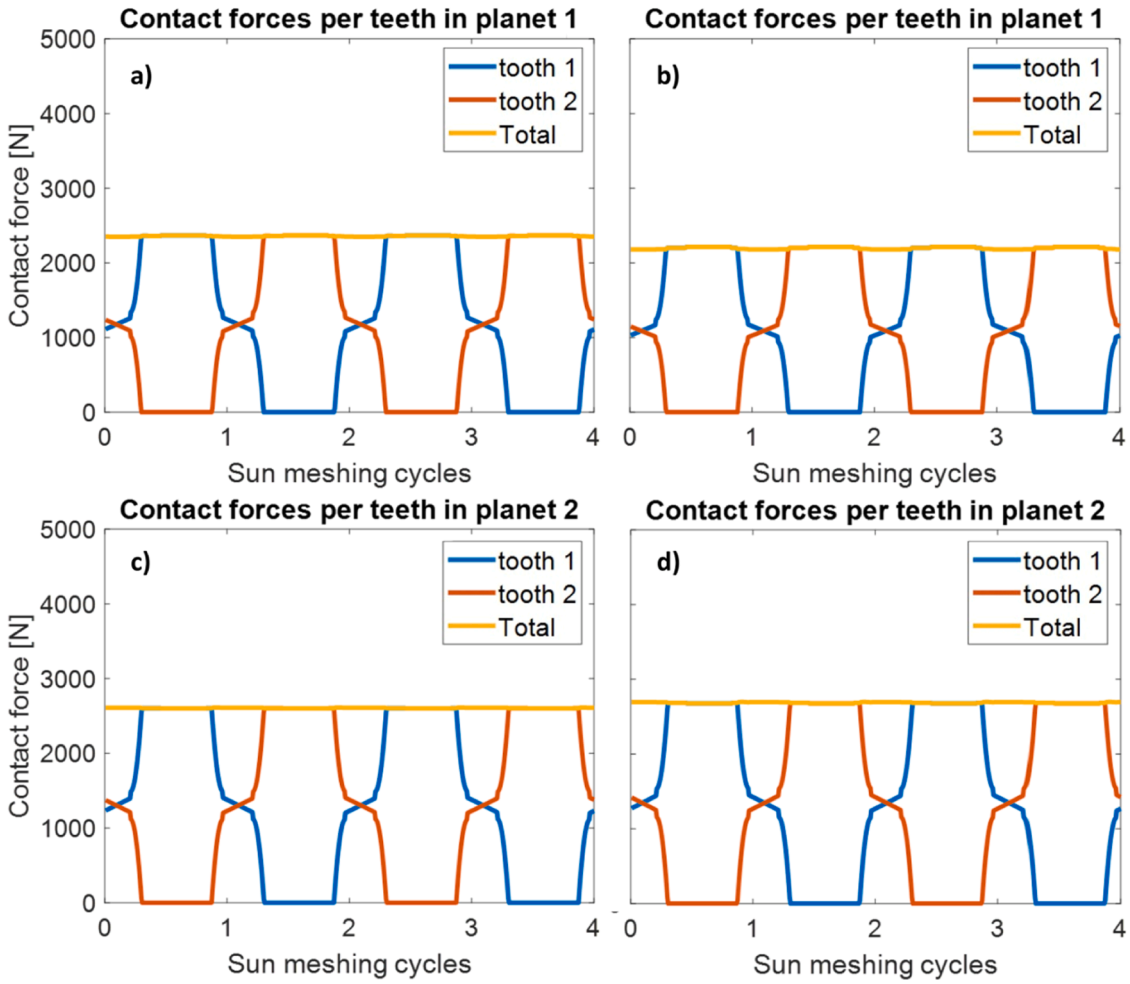


**Fig. 17.** 3-planet ESIP transmission 1e8 N/m (planet 1 & 2): a & c) 2.5 $\mu m$ b & d) 5 $\mu m$.

to infer the load sharing in a transmission from its orbit is the 5-planet ESSP transmission. Thus, the case without error, the case with 2.5 $\mu m$ and the case with 5 $\mu m$ are chosen and compared in Fig. 10. Furthermore, in Fig. 10 circles in dotted lines, with the same radius, are included to ease the comparison of the sizes of each loop described by the sun orbit. Besides, a sketch is included to show the initial position of the planets and the numbering used to refer to them.

In the case of no error, every loop is equal and so is the amount of load supported by each planet, however, with a delay due to the mesh phasing. On the contrary, in the second and third cases considering the position of each planet shown also in Fig. 10, it is possible to see that the loop related to planet 1 (the one with the error) becomes bigger due to the unloading related to the delaying tangential error. Then, the loops for planet 2 & 5 are smaller due to the higher stiffness in that area, these planets are overloaded. Finally, the two loops at the top, linked to planets 3 & 4 are bigger to the ones for 2 & 5, but smaller than the one for planet 1. These results are verified by the numerical results to the load sharing presented in Table 6. The variations in the loops are highlighted by including a circle in dotted line that is equally big for each scenario. This circle is centred on the centroid of each orbit. In the detail of each orbit (Fig. 10b), c) & d)) its centroid is included as $a +$ icon in red or green depending on the colour used for the orbit, the green colour is only used in the case the orbit is in red in order to improve the readability of Fig. 10. Finally, in Figs. 10–12 a sketch shows the starting position for each planet, following the numbering mentioned before in this work.

This is also visible for the orbits described by the sun in the 3-planet ESSP transmission, shown in Fig. 11, and the numerical values of the LSR are presented in Table 7. However, due to the self-balancing effect the imbalance created by the tangential error is not significant and this appears also in the uniformity of the orbit. Thus, the change of the orbits is presented and then the detail for 0, 2.5, and 5 $\mu m$. However, the variations in the orbits are slight, which is why the dotted circles, also included in Fig. 10, are more helpful in this new scenario and highlight the slight differences between orbits. The loops closer to the planet 2 & 3 become smaller and tighter. This may be due to the higher stiffness in this area. Likewise, the centroid is included in the representation of the detail of the orbits, as done before in Fig. 10. It is possible to observe the change in the position of this centroid with the change in the shape of the orbit.

The numerical values prove that the imbalances created in the 3-planet transmissions by the tangential errors are not as significant as in the 5-planet transmission.

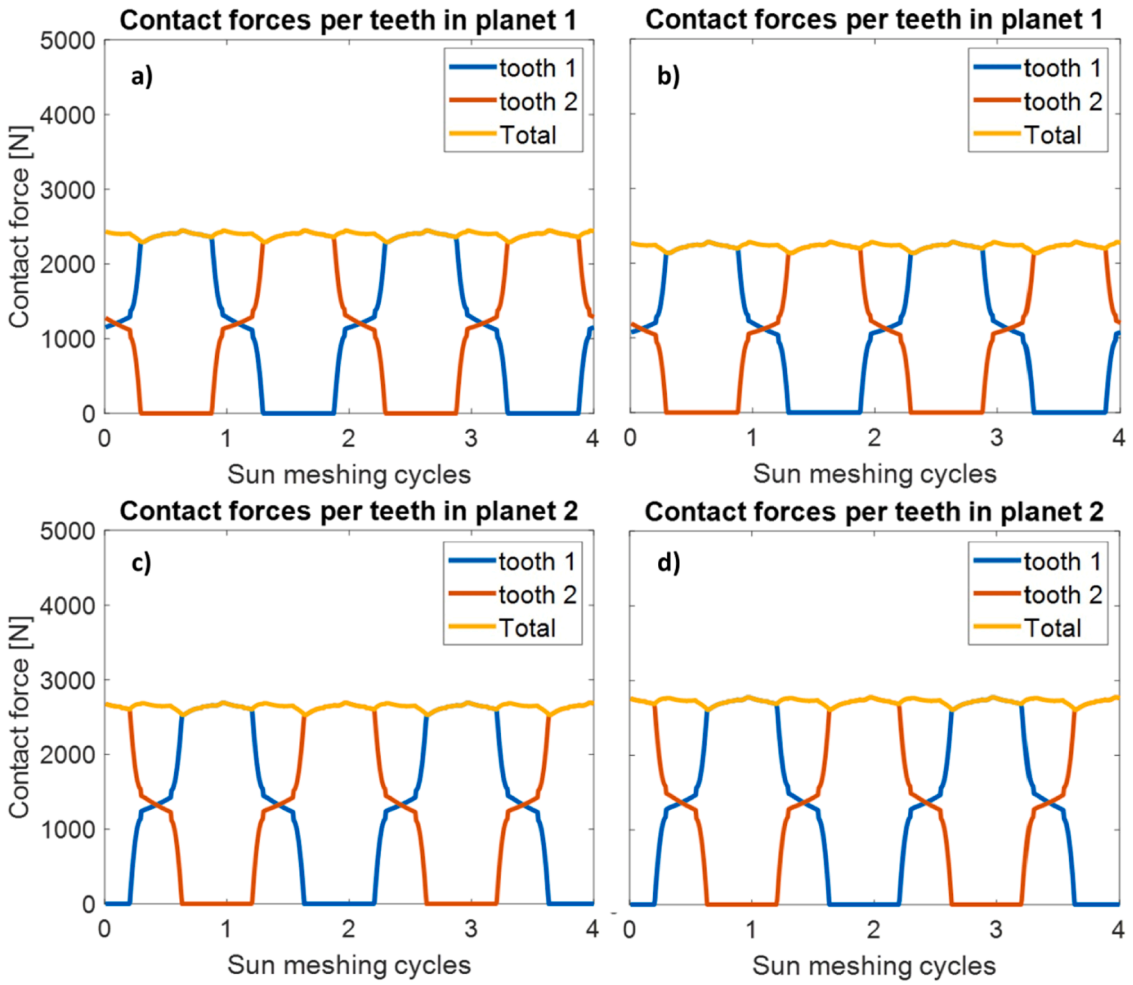


**Fig. 18.** 3-planet ESSP transmission 1e8 N/m (planet 1 & 2): a & c) 2.5 $\mu m$ b & d) 5 $\mu m$.

Regarding the 4-planet ESSP transmissions the analysis is more difficult due to the change in the shape of the orbit. The orbits are presented in Fig. 12 in two figures to avoid the overlap and ease the analysis. The results show that as the tangential error grows it is possible to see that the segments that go from planet 2–3 & 4–1 become shorter and the other become longer. This is related to the variation in the meshing stiffness due to the tangential error impact, which affects to the mobility of the sun. In these orbits all the scenarios are presented to observe the evolution of the orbit with the tangential error in more detail.

In the numerical values, compiled in Table 8 the trends shown in Fig. 12 are supported by the trends followed by the max.LSR results. Thus, the highest load corresponds to the planets where there is more stiffness and, therefore, the segments that start closer to these planets are shorter.

On the other hand, comparing the results among transmissions with varying number of planets, it is possible to see how the geometry affects the performance of the transmission. As shown in Fig. 13 the orbit described by the sun with the same stiffness in the support is smaller for a transmission with 3 or 5 planets, compared with an analogous 4-planet transmission. Even though the amount of load in the system is adapted to the number of planets, there seems to be an impact of the geometrical disposition of the planets in the size and shape of the orbit in ESSP transmissions.

Besides, in Fig. 13 it is possible to see the change in the shape with an even or odd number of planets.

Then, Fig. 14 shows the change in the position of the centroid of the orbit with the growth of the tangential pinhole position error. In this figure a number of dotted circles are included as reference for the size of the translation. Thus, it is possible to see how the sun gear orbit centroid suffers a higher translation for a 3-planet transmission. On the contrary, the centroid of the 5-planet transmission suffers the lowest translation with the tangential error, which is logical given the higher stiffness in the system due to the higher number of planets.

Finally, the stiffness in the support also plays an important role in the orbits. Reducing the stiffness of the sun support influences the size of the orbit and the translation suffered by the centre of the orbit, as shown in Fig. 15.

This stands for any number of planets. Also, it is possible to see how the closer the sun gets to a planet (for example planet 2 in the 5-

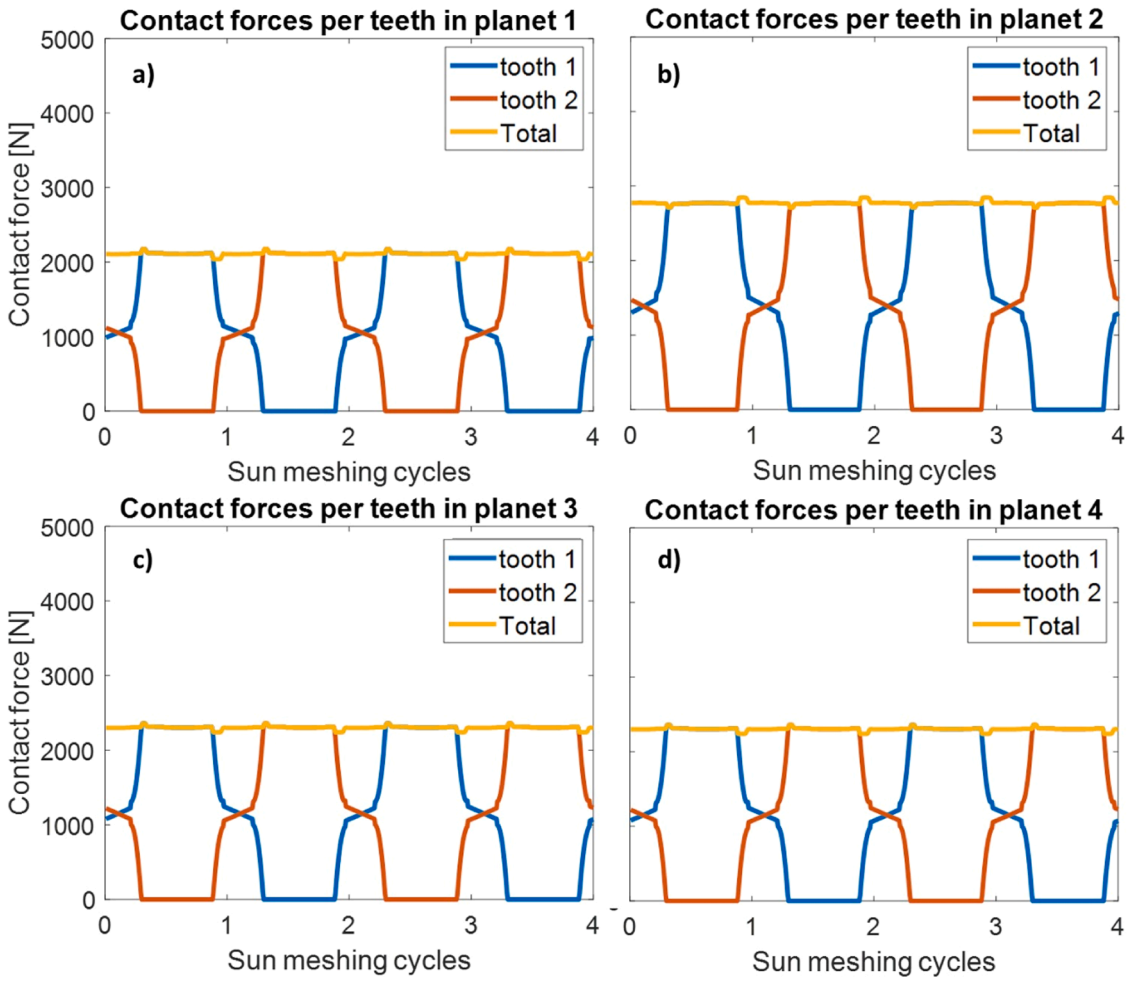


**Fig. 19.** 4-planet ESIP transmission 1e8 N/m for every planet with a 2.5 $\mu m$ error.

planet ESSP transmission) the more distorted the orbit is in that area becoming flatter and wider.

### 4.2. *Contact forces*

Starting off the ideal scenario where there is no error and the load is shared equally among every planet, Fig. 16 shows a comparison of this scenario for 3, 4 and 5-planet ESIP and ESSP transmissions. This is the starting point of this study.

In the case for the ESIP transmissions (Fig. 16a, b & c), every tooth supports the same load in the same way and the summation, which would be used for the load sharing, is perfectly uniform and equal for every planet. On the contrary, for ESSP transmissions, in Fig. 16d, e, & f, every planet supports the same load but delayed in time, due to the mesh phasing. Thus, there exist fluctuations in the load and the amount of load supported by a tooth alone is not the same as for both teeth at the same time.

It is worth highlighting the significant change (seen in Fig. 16) that exists in the peak-to-peak value of the contact forces for ESSP transmissions as the number of planets is changed. This has to be considered bearing in mind that these are ideal transmissions with no error and a 1e8 N/m stiffness in the sun support in all of them.

Focusing on the scenario with 3 planets for the ESIP configuration and for the ESSP configuration the contact forces with a 2.5 and 5 $\mu$m tangential errors are gathered in Figs. 17 and 18. Thus, in Fig. 17a & b it is possible to observe the loads in planet 1. Whereas Fig. 17c & d show the same scenario, but for planet 2. This comparison proves the change in the total load and in the maximum load borne by a tooth with the change of the size in the error. However, this difference is small due to the effect of the stiffness in the sun support. Therefore, it can be extrapolated that for a lower stiffness these differences would get smaller, justifying the decision to neglect the simulations of 3-planet transmissions with 1e6 N/m stiffness in the sun support. However, this is a characteristic inherent to the 3-planet transmissions.

On the other hand, in 4-planet transmissions the tangential error plays a different role. For the ESIP transmission, the tangential error generates a delay in the contact in planet 1. Besides, this underloads that planet and overloads other planets, as shown in Fig. 19, which modifies the amount of pairs of teeth in contact in each planet. The results show that the planet 1 and planet 2 are the most

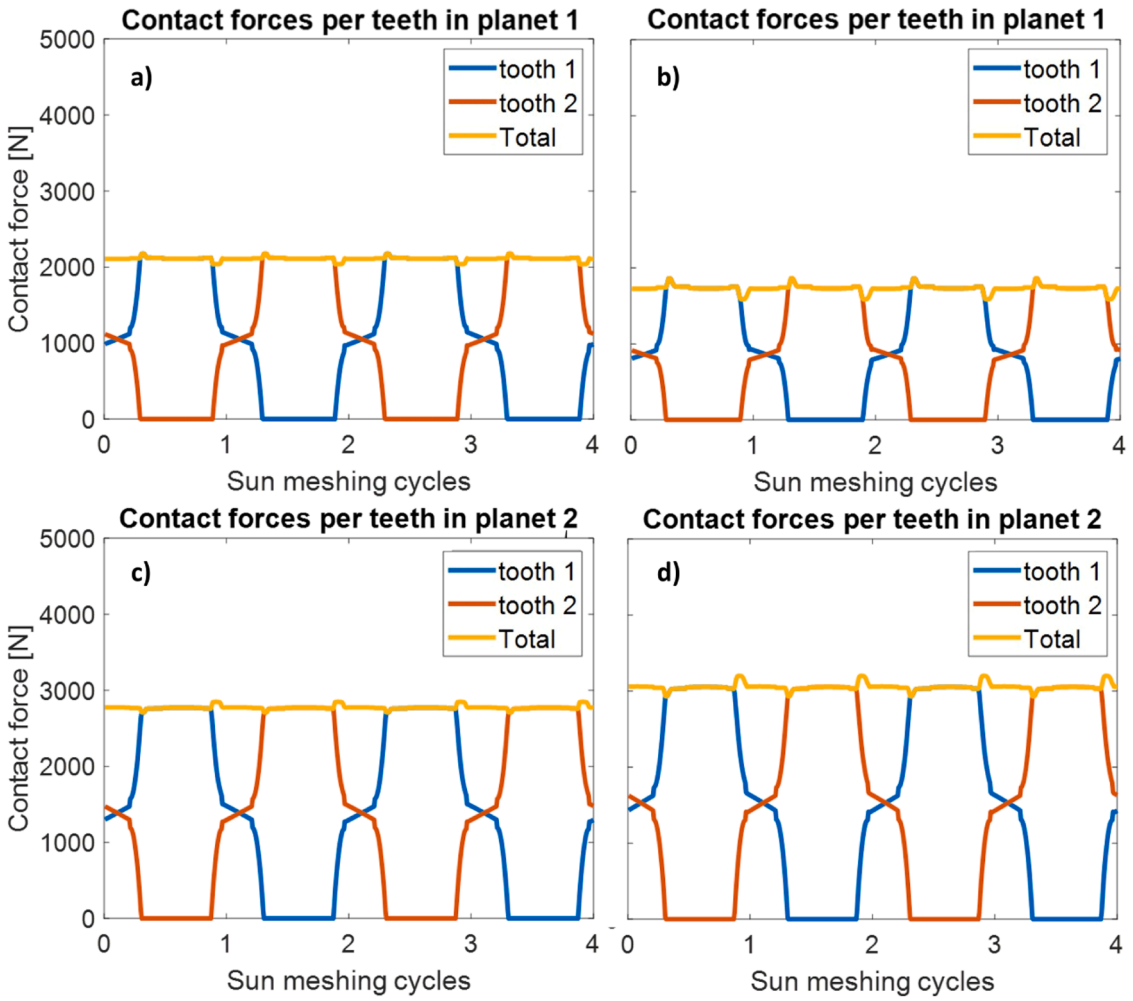


**Fig. 20.** 4-planet ESIP transmissions 1e8 N/m (planet 1 & 2): a & c) 2.5 $\mu m$ b & d) 5 $\mu m$.

underloaded and overloaded respectively. Hence, the results for these planets are extracted and compared for the scenarios with a 2.5 & 5 $\mu m$ error, as shown in Fig. 20.

The change in the number of pairs of teeth in contact appears in the contact forces represented by the fluctuations that can be observed in the transition sections, which are the ones where the contact goes from single to double and vice versa.

In the case of the ESSP transmission, the contact forces for the planet 1 & 2 are the most relevant too. Therefore, they are extracted in order to compare them in Fig. 21. In those, there are fluctuations in the load due to the sequential mesh phasing. For the 1e8 N/m stiffness these fluctuations lead to 2 maximum load values in any load cycle in each tooth. However, the maximum load corresponds to a moment where the load is distributed among both teeth in contact. Therefore, this moment sets the maximum in the load sharing in this planet, but it is not representative of the highest overload borne by a single tooth. This stands for all the error sizes considered.

On the other hand, whenever the stiffness in the sun support is lowered to 1e6 N/m (Fig. 22), the maximum values in the load are equal for the single and double contact and it corresponds to a value that is higher in the single contact and lower in the double contact in the 1e8 stiffness scenarios.

Finally, for 5-planet transmissions, the planet 1, with the error, experiments an underloading effect and there is an overloading effect in the 2nd planet. Given this, in Fig. 23 the contact forces in planet 1 & 2 are gathered for the scenarios with 1.25, 3.75 and 5 $\mu m$ errors. These show that the moment of highest load in planet 1 corresponds to a single contact. On the other hand, in planet 2 the highest load is supported by two teeth at the same time. Thus, the overload due to the error in the planet does not mean an identical overload in the tooth. Even though in planet 1 the maximum load is borne by a single contact, the tooth is underloaded due to the effect of the tangential error.

Besides, comparing the behavior seen in Fig. 23 with the previous Figs. 21 and 22, in the 5-planet ESIP transmission the error does modify the contact force peak-to-peak value notably. On the other hand, in the ESSP transmissions presented before (Figs. 21 and 22) this effect is not visible. As a matter of fact, this happens also for the 5-planet ESSP transmission, whose results are presented in Fig. 24.

Also for 5-planet transmissions, but with sequential mesh phasing, the tangential pinhole position errors have a significant

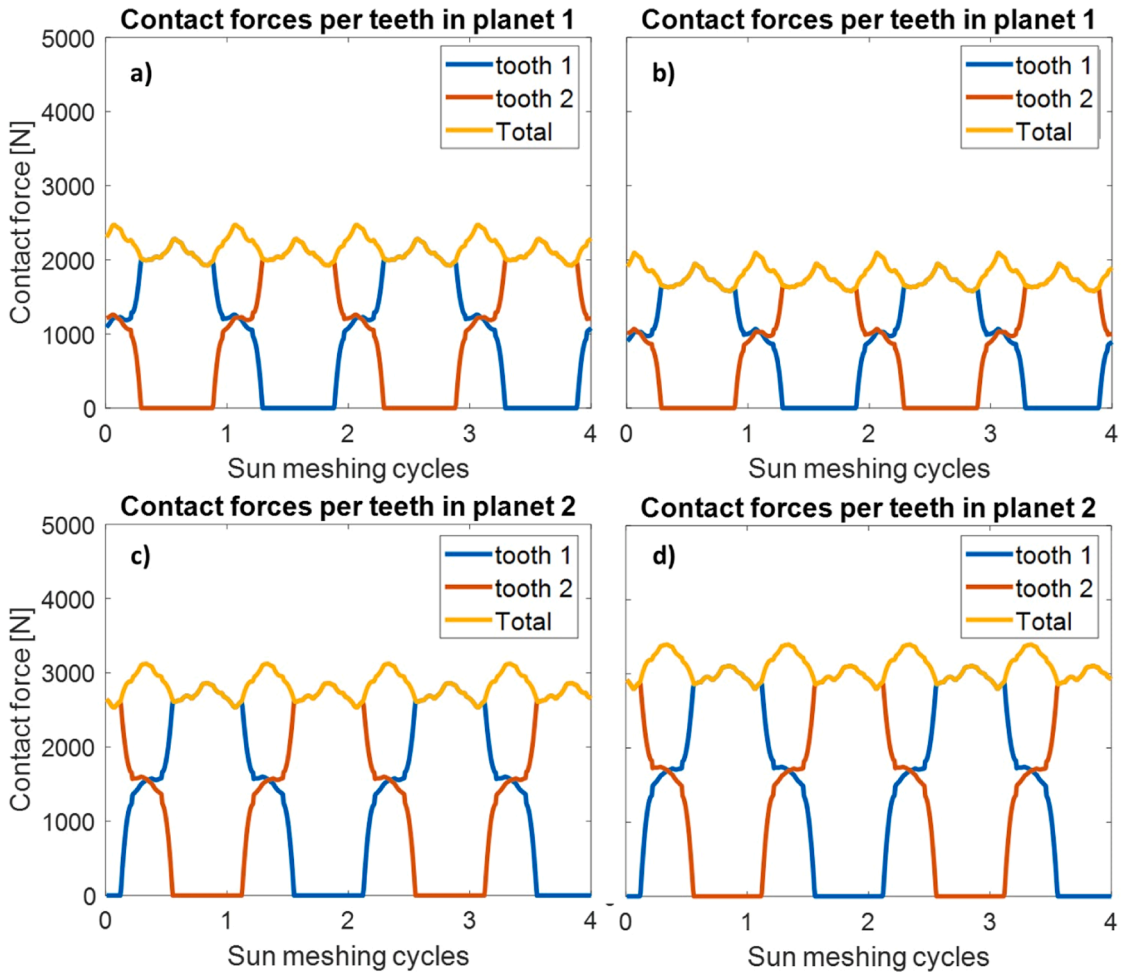


**Fig. 21.** 4-planet ESSP transmissions 1e8 N/m (planet 1 & 2): a & c)2.5 $\mu m$ b & d) 5 $\mu m$.

influence. However, as done previously, the focus is set on the planet 1 & 2 due to the mentioned underloading and overloading effect (Fig. 24). Thus, in these results the effects that can be identified, compared to the analogous ESIP transmission, are different due to the sequential mesh phasing. Firstly, there is a fluctuation of the load in the planet that provides almost identical values for the maximum load supported in a single contact and in a double contact. This effect has an important impact in the durability of the components given the increment in the number of cycles supported by each tooth.

As seen for 4-planet ESSP transmissions, the reduction in the stiffness in the sun support results in more uniform loads in the 5-planet transmissions, compared with the analogous scenario with a 1e8 N/m stiffness. Thus, Fig. 25 shows this effect for the scenarios with 1.25, 3.75 and 5 $\mu m$ tangential error. The variability in the loads is reduced due to the lower stiffness, however, the number of cycles does not vary.

All in all, the effect of the tangential position errors and the stiffness in the sun support can be analysed by using Fig. 26. These present the comparison between the highest load supported by a single contact (identified as SC) and the maximum load borne by a planet, this could be by a single or double contact. Thus, it is possible to see that for ESIP transmissions with 4 or 5 planets the amount of load supported by the wheel is higher than the one supported by a single contact. Therefore, the load sharing is not an accurate indicator in this case, at least for the amount of overload that a single tooth has to bear in this scenario. Then, in the case of the ESSP transmissions the discrepancies between both magnitudes almost disappear with the variation of the sun support stiffness.

Therefore, with all the results presented, it is possible to prove the hypothesis presented and observe the discrepancies between the load supported by a planet and the real load supported by a tooth alone.

## 5. Conclusions

Regarding the analysis of the orbits described by the sun gear and the contact forces, the following conclusions can be extracted:

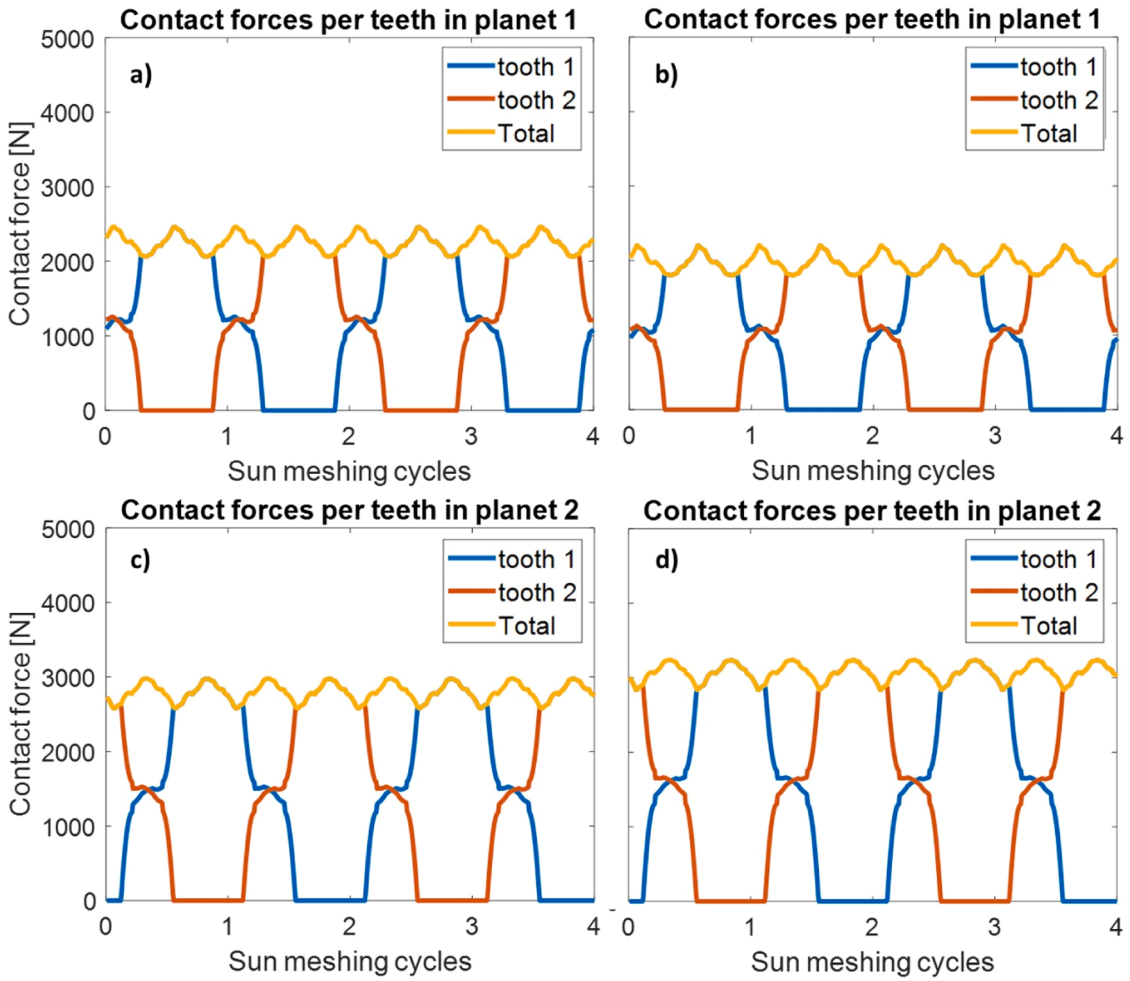


**Fig. 22.** 4-planet ESSP transmissions 1e6 N/m (planet 1 & 2): a & c) 2.5 $\mu m$ b & d) 5 $\mu m$.

- The new representation of the orbits, presented in this work, allows to observe the load sharing ratio in ESSP transmissions. Besides, it allows to perceive differences between meshing cycles, thus, it provides the opportunity of detecting the effect of time-varying errors. However, this technique proves to be less accurate than others, on the contrary, its simplicity is an advantage.
- The imbalance created in the planetary transmission load sharing by tangential pinhole position errors does not affect in the same way the load per tooth and the LSR. The LSR shows the maximum load per tooth in the underloaded planets, whereas it shows the maximum load borne by a double contact in the overloaded ones. Therefore, it does not provide crucial information regarding the load per tooth and the amount of load borne by an overloaded single contact.
- As the freedom in the sun support grows, so does the load borne by a single contact and tends to equalize the load borne by a double contact in any planet.
- As the size of the error grows, so does the difference between the load borne by a single and a double contact, in relative terms to the average load borne by the wheel.
- The variability of the load per tooth in ESSP transmissions completes more cycles than in an ESIP transmission. This may have an impact in the durability of the teeth given the higher load supported by planets in ESSP transmissions and the higher number of load cycles by meshing cycle.

## Declaration of Competing Interest

The authors declare that they have no known competing financial interests or personal relationships that could have appeared to influence the work reported in this paper.

## Data availability

The data has been disclosed in the manuscript, but the code will not be disclosed.

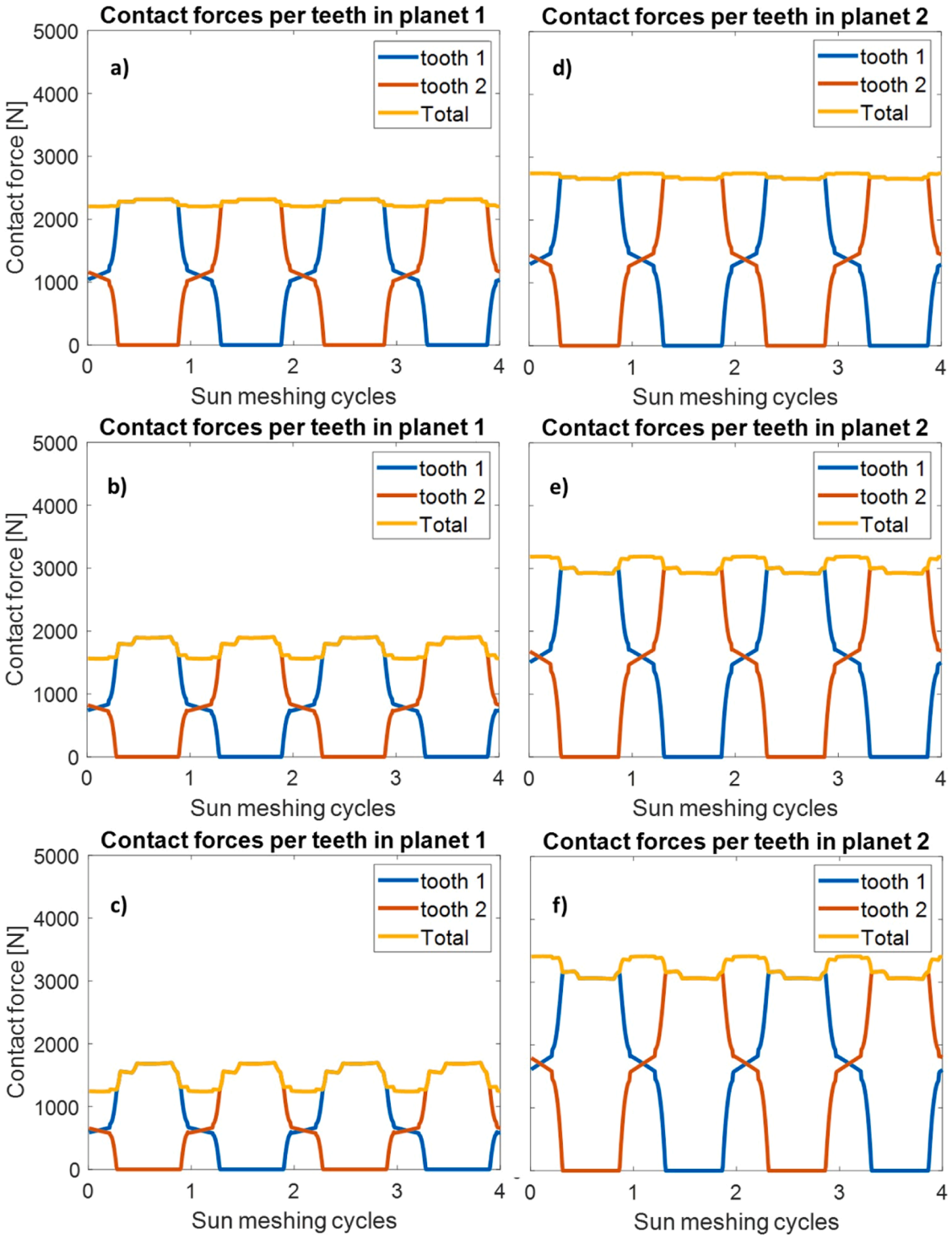


**Fig. 23.** 5-planet ESIP transmissions 1e8 N/m (planet 1 & 2): a & d) 1.25 $\mu m$ b & e) 3.75 $\mu m$ c & f) 5 $\mu m$.

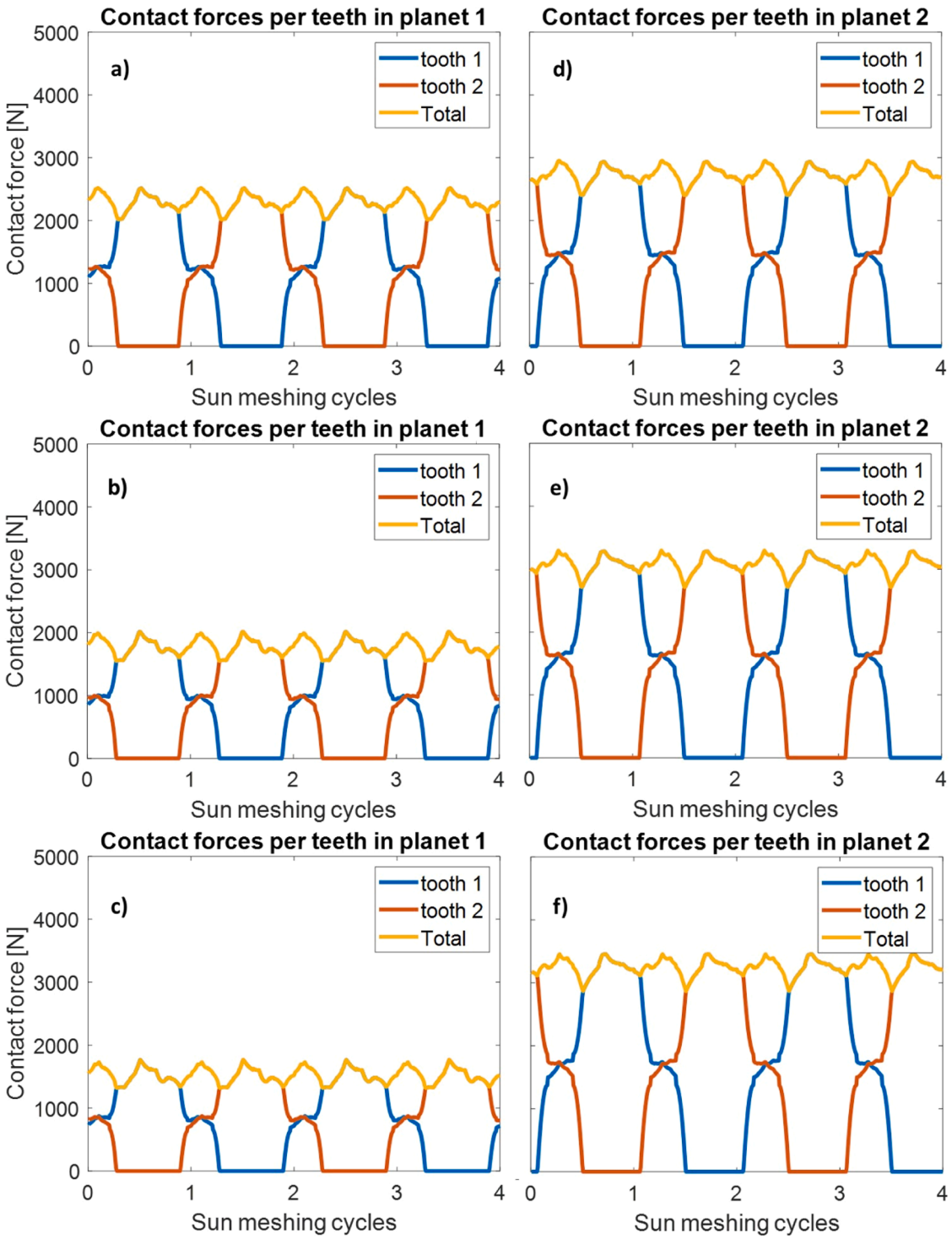


**Fig. 24.** 5-planet ESSP 1e8 N/m (planet 1 & 2): a & d)1.25 $\mu m$ b & e) 3.75 $\mu m$ c & f) 5 $\mu m$.

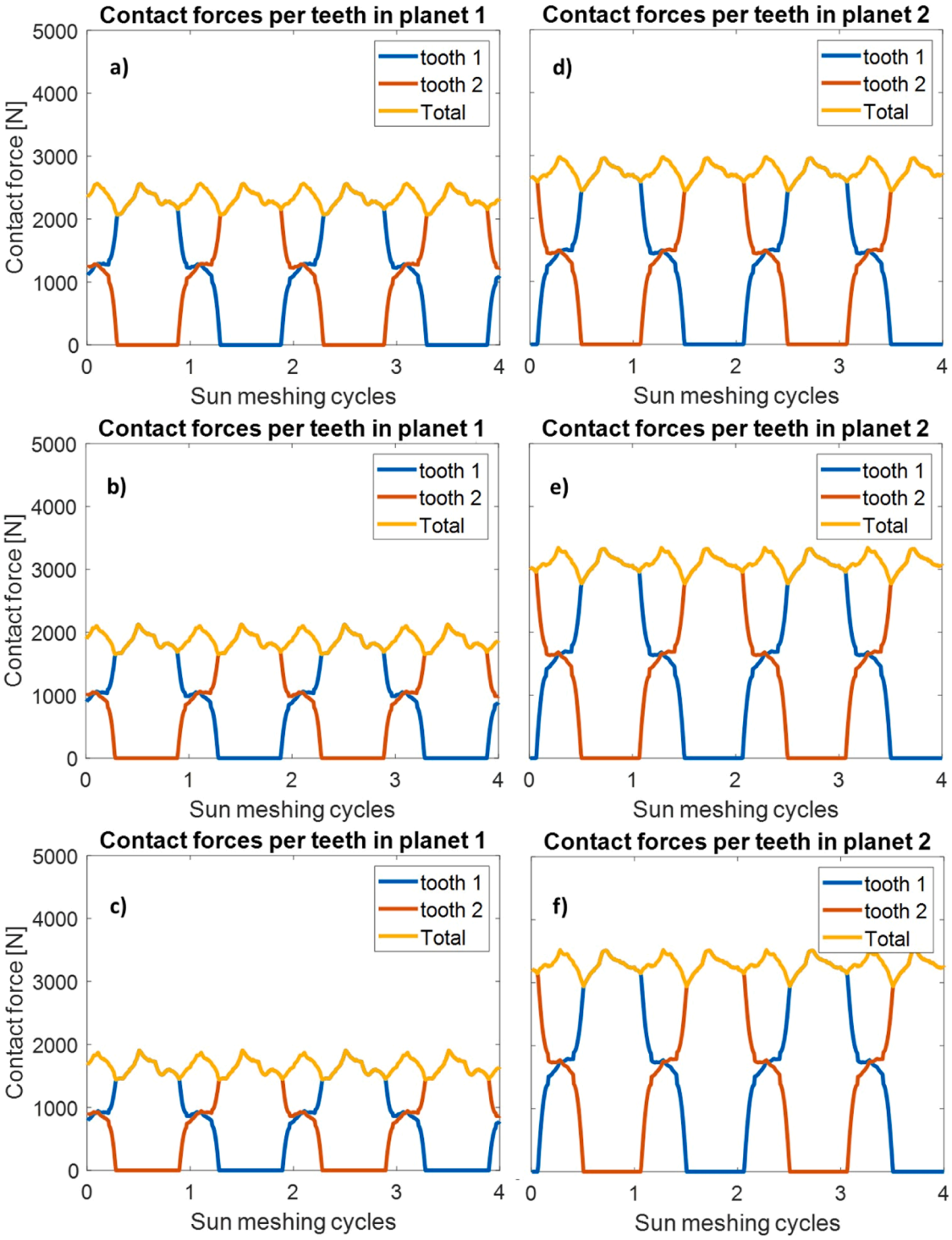


**Fig. 25.** 5-planet ESSP 1e6 N/m (planet 1 & 2): a & d)1.25 $\mu m$ b & e) 3.75 $\mu m$ c & f) 5 $\mu m$.

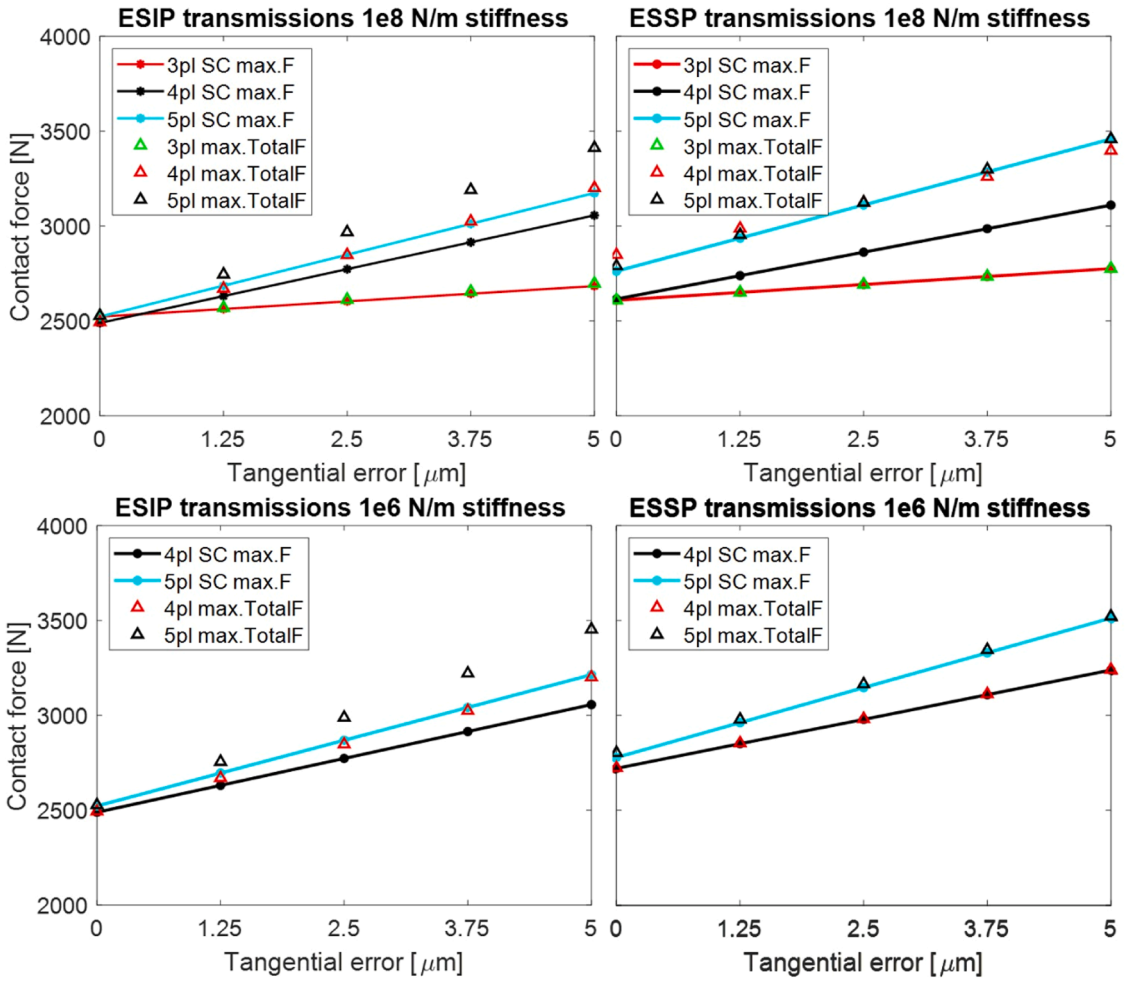


**Fig. 26.** Comparison of the forces supported in single contact and by the whole wheel.

## Acknowledgments

The authors would like to acknowledge Project DPI2017-85390-P funded by the Spanish Ministry of Economy, Industry, and Competitiveness for supporting this research. Moreover, the authors acknowledge the Project PID2020-116213RB-I00 funded by the Ministry of Science and Innovation.

## References

[1] F. Viadero, A. Fernandez, M. Iglesias, A. De-Juan, E. Liaño, M.A. Serna, Non-stationary dynamic analysis of a wind turbine power drivetrain: offshore considerations, Appl. Acoust. 77 (2014) 204–211.
[2] J. Tan, C. Zhu, C. Song, Y. Li, X. Xu, Dynamic modeling and analysis of wind turbine drivetrain considering platform motion, Mech. Mach. Theory 140 (2019) 781–808.
[3] W. Du, S. Zhao, L. Jin, J. Gao, Z. Zheng, Optimization design and performance comparison of different powertrains of electric vehicles, Mech. Mach. Theory 156 (2021), 104143.
[4] D.M. Blunt, J.A. Keller, Detection of a fatigue crack in a UH-60A planet gear carrier using vibration analysis, Mech. Syst. Signal Process. 20 (Nov 2006) 2095–2111.
[5] M. Botman, Vibration measurements on planetary gears of aircraft turbine engines, J. Aircr. 17 (5) (1980) 351–357.
[6] C.G. Cooley, R.G. Parker, A review of planetary and epicyclic gear dynamics and vibrations research, Appl. Mech. Rev. 66 (4) (2014), 040804.
[7] M. Maatar, P. Velex, An analytical expression for the timevarying contact length in perfect cylindrical gears: some possible applications in gear dynamics, J. Mech. Des. 118 (Dec 1996) 586–589.
[8] A. Kahraman, Load sharing characteristics of planetary transmissions, Mech. Mach. Theory 29 (8) (1994) 1151–1165.
[9] J.I. Pedrero, D. Martinez-Lopez, J. Calvo-Irisarri, M. Pleguezuelos, M.B. Sanchez, A. Fernandez-Sison, Minimum friction losses in wind turbine gearboxes, Forschung im Ingenieurwesen/Engineering Research (2021).
[10] J.I. Pedrero, M. Pleguezuelos, M.B. Sanchez, Influence of meshing stiffness on load distribution between planets of planetary gear drives, Mech. Mach. Theory 170 (November 2021) 2022.
[11] W. Liu, J. Li, Y. Kang, Y. Liu, X. Xu, P. Dong, Load sharing behavior of double-pinion planetary gear sets considering manufacturing errors, IOP Conferen. Ser.: Mater. Sci. Eng. 677 (5) (2019).

[12] L. Ryali, D. Talbot, A dynamic load distribution model of planetary gear sets, Mech. Mach. Theory 158 (Apr 2021), 104229.
[13] M.B. Sanchez, M. Pleguezuelos, J.I. Pedrero, Influence of profile modifications on meshing stiffness, load sharing, and transmission error of involute spur gears, Mech. Mach. Theory 139 (2019) 506–525.
[14] S. Shweiki, D. Mundo, J. Korta, P. Oranges, A. Palermo, Investigation of mesh phasing in a planetary gear train using combined FE and multibody simulations, Isma (2016) 1407–1416.
[15] J. Brauer, A general finite element model of involute gears, Finite Elem. Analy. Des. 40 (Aug 2004) 1857–1872.
[16] T.M. Ericson, R.G. Parker, Experimental measurement and finite element simulation of elastic-body vibration in planetary gears, Mech. Mach. Theory 160 (Jun 2021), 104264.
[17] V. Abousleiman, P. Velex, A hybrid 3D finite element/lumped parameter model for quasi-static and dynamic analyses of planetary/epicyclic gear sets, Mech. Mach. Theory 41 (6) (2006) 725–748.
[18] A. Fernandez del Rincon, F. Viadero, M. Iglesias, P. Garcıa, R. Sancibrian, A model for the study of meshing stiffness in spur gear transmissions, Mech. Mach. Theory 61 (2013) 30–58.
[19] M. Iglesias, A. Fernandez del Rincon, A. De-Juan, A. Diez-Ibarbia, P. Garcia, F. Viadero, Advanced model for the calculation of meshing forces in spur gear planetary transmissions, Meccanica 50 (7) (2015) 1869–1894.
[20] C. Zhang, J. Wei, F. Wang, S. Hou, A. Zhang, T.C. Lim, Dynamic model and load sharing performance of planetary gear system with journal bearing, Mech. Mach. Theory 151 (Sep 2020), 103898.
[21] S. Portron, P. Velex, V. Abousleiman, A hybrid model to study the effect of tooth lead modifications on the dynamic behavior of double helical planetary gears, Proceed. Instit. Mech. Eng., Part C: J. Mech. Eng. Sci. 233 (21–22) (2019) 7224–7235.
[22] M. Pleguezuelos, M.B. Sanchez, J.I. Pedrero, Analytical model for meshing stiffness, load sharing, and transmission error for spur gears with profile modification under non-nominal load conditions, Appl. Math. Model. 97 (2021) 344–365.
[23] H. Dai, X. Long, F. Chen, C. Xun, An improved analytical model for gear mesh stiffness calculation, Mech. Mach. Theory 159 (2021), 104262.
[24] Z. Chen, Z. Zhou, W. Zhai, K. Wang, Improved analytical calculation model of spur gear mesh excitations with tooth profile deviations, Mech. Mach. Theory 149 (2020), 103838.
[25] C. Yuksel, A. Kahraman, Dynamic tooth loads of planetary gear sets having tooth profile wear, Mech. Mach. Theory 39 (7) (2004) 695–715.
[26] D. Xiang, Y. Shen, Y. Wei, A contact force model considering meshing and collision states for dynamic analysis in Helical gear system, Chin. J. Mech. Eng. (Engl. Ed.) 32 (1) (2019) 1–12.
[27] A. Fingerle, M. Otto, K. Stahl, Definition of a coefficient to evaluate a moving contact pattern in planetary gearboxes, Forschung im Ingenieurwesen/Engineering Research 84 (3) (2020) 235–243.
[28] A. Bodas, A. Kahraman, Influence of carrier and gear manufacturing errors on the static load sharing behavior of planetary gear sets, JSME Int. J. Ser. C 47 (3) (2004) 908–915.
[29] A. Singh, Load sharing behavior in epicyclic gears: physical explanation and generalized formulation, Mech. Mach. Theory 45 (3) (2010) 511–530.
[30] N. Driot, E. Rigaud, J. Perret-Liaudet, Gdn-12 variability of critical rotational speeds of gearbox induced by misalignment and manufacturing errors(gear dynamics and noise), Proceed. JSME Int. Conferen. Motion Power Transmiss. (2001) 63–67, vol. I.01.202, no. 0.
[31] E. Caso, A. Fernandez-del Rincon, P. Garcia, M. Iglesias, F. Viadero, Monitoring of misalignment in low speed geared shafts with acoustic emission sensors, Appl. Acoust. 159 (Feb 2020), 107092.
[32] Z. Liu, Z. Liu, X. Yu, Dynamic modeling and response of a spur planetary gear system with journal bearings under gravity effects, J. Vibra. Control 24 (Aug 2018) 3569–3586.
[33] A. Hammami, M.I. Santamaria, A.F. Del Rincon, F. Chaari, F.V. Rueda, M. Haddar, Load Sharing Behavior in Planetary Gear Set, in, Appl. Condition Monitor. 2 (2015) 459–468.
[34] Y. Guo, R.G. Parker, Dynamic modeling and analysis of a spur planetary gear involving tooth wedging and bearing clearance nonlinearity, Eur. J. Mech. - A/Solid. 29 (Nov 2010) 1022–1033.
[35] A. Fernandez-del-Rincon, M. Iglesias, A. De-Juan, A. Diez-Ibarbia, P. Garcıa, F. Viadero, Gear transmission dynamics: effects of index and run out errors, Appl. Acoust. 108 (2016) 63–83.
[36] Y. Hu, D. Talbot, A. Kahraman, A load distribution model for planetary gear sets, J. Mech. Des. 140 (5) (2018), 053302.
[37] S. Mo, Y. Zhang, Q. Wu, S. Matsumura, H. Houjoh, Load sharing behavior analysis method of wind turbine gearbox in consideration of multiple-errors, Renew. Energy 97 (Nov 2016) 481–491.
[38] M. Iglesias, A. Fernandez del Rincon, A. De-Juan, P. Garcia, A. Diez-Ibarbia, F. Viadero, Planetary transmission load sharing: manufacturing errors and system configuration study, Mech. Mach. Theory 111 (May 2017) 21–38.
[39] D.-p. Sheng, R.-p. Zhu, G.-h. Jin, F.-x. Lu, H.-y. Bao, Dynamic load sharing characteristics and sun gear radial orbits of double-row planetary gear train, J. Centr. South Univ. 22 (Oct 2015) 3806–3816.
[40] R. August, R. Kasuba, Torsional vibrations and dynamic loads in a basic planetary gear system, J. Vib. Acoust. 108 (Jul 1986) 348–353.
[41] B. Boguski, A. Kahraman, T. Nishino, A new method to measure planet load sharing and sun gear radial orbit of planetary gear sets, J. Mech. Des. 134 (Jul 2012), 071002.
[42] J. Götz, F. Siglmüller, M. Fürst, M. Otto, K. Stahl, Experimental investigation of the dynamic load sharing of planetary gearboxes, Forschung im Ingenieurwesen (Jul 2021).
[43] H. Dai, F. Chen, C. Xun, X. Long, Numerical calculation and experimental measurement for gear mesh force of planetary gear transmissions, Mech. Syst. Signal Process. 162 (Jan 2022), 108085.
[44] H. Aurrekoetxea, I.R.D. Ocenda, Experimental and theoretical study of load mesh factor for different boundary conditions in wind gearbox planetary stages, in, in: International Conference on Gears 2019, VDI Verlag, 2019, pp. 835–844.
[45] U.G. Santiago, A.F. Sison, H. Polinder, J.-.W. van Wingerden, Experimental evaluation of the mesh load factor ($K_\gamma$) of a 6MW wind turbine gearbox, J. Phys.: Conferen. Ser. 2265 (3) (2022), 032003.
[46] A. Singh, A. Kahraman, H. Ligata, Internal gear strains and load sharing in planetary transmissions: model and experiments, J. Mech. Des. 130 (7) (2008), 072602.
[47] J. Sanchez-Espiga, A. Fernandez-del Rincon, M. Iglesias, F. Viadero, Planetary gear transmissions load sharing measurement from tooth root strains: numerical evaluation of mesh phasing influence, Mech. Mach. Theory 163 (Sep 2021), 104370.
[48] J. Sanchez-Espiga, A. Fernandez-del Rincon, M. Iglesias, F. Viadero, Numerical evaluation of the accuracy in the load sharing calculation using strain gauges: sun and ring gear tooth root, Mech. Mach. Theory 175 (Sep 2022), 104923.
[49] K. Weber, C. Banaschek, The Deformation of Loaded Gears and the Effect On Their Load Carrying Capacity, 1951.
[50] J. Sanchez-Espiga, A. Fernandez-del Rincon, M. Iglesias, F. Viadero, Influence of the phase in planetary gears load sharing and transmission error, in, Mech. Mach. Sci. 73 (2019) 1059–1067.
[51] J. Sanchez-Espiga, A. Fernandez-del Rincon, M. Iglesias, F. Viadero, Influence of errors in planetary transmissions load sharing under different mesh phasing, Mech. Mach. Theory 153 (Nov 2020), 104012.
[52] A. Singh, Application of a System Level Model to Study the Planetary Load Sharing Behavior, J. Mech. Des. 127 (May 2005) 469–476.